Acta Pharmaceutica Sinica B 2024;14(4):1605−1623

Chinese Pharmaceutical Association
Institute of Materia Medica, Chinese Academy of Medical Sciences

Acta Pharmaceutica Sinica B

www.elsevier.com/locate/apsb
www.sciencedirect.com

ORIGINAL ARTICLE

FGF4 protects the liver from immune-mediated injury by activating CaMKKβ-PINK1 signal pathway to inhibit hepatocellular apoptosis

Zhifeng Huang[a,b,*,†], Tongtong Pan[a,*,†], Liang Xu[c,†], Lu Shi[b,†], Xiong Ma[d], Liya Zhou[b], Luyao Wang[b], Jiaojiao Wang[a,b], Guoqing Zhu[a], Dazhi Chen[e], Lingtao Song[b], Xiaomin Pan[b], Xiaodong Wang[a], Xiaokun Li[b], Yongde Luo[a,b], Yongping Chen[a,*]

[a]*Hepatology Diagnosis and Treatment Center, Zhejiang Provincial Key Laboratory for Accurate Diagnosis and Treatment of Chronic Liver Diseases, the First Affiliated Hospital of Wenzhou Medical University, Wenzhou 325035, China*
[b]*Oujiang Laboratory (Zhejiang Lab for Regenerative Medicine, Vision and Brain Health) & School of Pharmaceutical Sciences, Wenzhou Medical University, Wenzhou 325035, China*
[c]*School of Laboratory Medicine and Life Sciences, Wenzhou Medical University & Key Laboratory of Laboratory Medicine, Ministry of Education, Wenzhou Medical University, Wenzhou 325035, China*
[d]*Division of Gastroenterology and Hepatology, Key Laboratory of Gastroenterology and Hepatology, Ministry of Health, State Key Laboratory for Oncogenes and Related Genes, Renji Hospital, School of Medicine, Shanghai Jiao Tong University, Shanghai 200001, China*
[e]*Hangzhou Medical College, Hangzhou 311300, China*

Received 26 October 2023; received in revised form 11 December 2023; accepted 15 December 2023

KEY WORDS

Fibroblast growth factor 4;
Fibroblast growth factor receptor 4;
Immune liver injury;
Ca^{2+}/Calmodulin dependent protein

Abstract Immune-mediated liver injury (ILI) is a condition where an aberrant immune response due to various triggers causes the destruction of hepatocytes. Fibroblast growth factor 4 (FGF4) was recently identified as a hepatoprotective cytokine; however, its role in ILI remains unclear. In patients with autoimmune hepatitis (type of ILI) and mouse models of concanavalin A (ConA)- or S-100-induced ILI, we observed a biphasic pattern in hepatic FGF4 expression, characterized by an initial increase followed by a return to basal levels. Hepatic FGF4 deficiency activated the mitochondria-associated intrinsic apoptotic pathway, aggravating hepatocellular apoptosis. This led to intrahepatic immune hyper-reactivity,

*Corresponding authors.
E-mail addresses: hzf@wmu.edu.cn (Zhifeng Huang), ptt_wmu@163.com (Tongtong Pan), cyp@wmu.edu.cn (Yongping Chen).
†These authors made equal contributions to this work.
Peer review under the responsibility of Chinese Pharmaceutical Association and Institute of Materia Medica, Chinese Academy of Medical Sciences.

https://doi.org/10.1016/j.apsb.2023.12.012

kinase 2;
PTEN-induced putative kinase 1;
Mitochondria-associated apoptosis

inflammation accentuation, and subsequent liver injury in both ILI models. Conversely, administration of recombinant FGF4 reduced hepatocellular apoptosis and rectified immune imbalance, thereby mitigating liver damage. The beneficial effects of FGF4 were mediated by hepatocellular FGF receptor 4, which activated the Ca^{2+}/calmodulin-dependent protein kinasekinase 2 (CaMKKβ) and its downstream phosphatase and tensin homologue-induced putative kinase 1 (PINK1)-dependent B-cell lymphoma 2-like protein 1-isoform L (Bcl-X_L) signalling axis in the mitochondria. Hence, FGF4 serves as an early response factor and plays a protective role against ILI, suggesting a therapeutic potential of FGF4 and its analogue for treating clinical immune disorder-related liver injuries.

1. Introduction

Immune liver injury (ILI), which is caused by various factors such as viruses, alcohol, drugs, chemicals, and immune dysregulation, continues to be a global health problem as it has the potential to result in liver failure and even death[1–3]. In recent years, the incidence of ILI has increased dramatically in the United States, Europe, and Asia[4]. On the cellular level, ILI is characterised by immune disorder-associated immune cell infiltration, progressive hepatic necro-inflammation, hepatocellular death, and tissue destruction (*e.g.*, fibrotic scarring)[5,6]. Liver biopsies from patients with ILI often show the formation of a characteristic apoptosome known as the "Councilman body"[7]. Despite the current understanding that hepatocellular apoptosis is a key trigger of disease progression[5,6], the mechanism underlying ILI pathogenesis still remains obscure. Currently, ILI is typically treated with immunosuppressive agents, such as prednisolone/budesonide and azathioprine. However, these agents also exert adverse side-effects including immunity impairment and endocrine system disturbance[1,3,8]. Therefore, there is an urgent need for safer and more effective pharmacotherapies.

The human fibroblast growth factor (FGF) family consists of 18 members that regulate paracrine and endocrine pathways by activating different isoforms of the cognate membrane-spanning FGF receptor (FGFR) tyrosine kinase family[9,10]. Ye et al. found that in response to liver injury induced by acetaminophen- or *N*-acetyl-*p*-aminophenol (APAP) hepatic expression of FGF21 was induced, peaking at 3 h for mRNA levels and 6 h for serum protein levels, before returning to basal levels 24 h after APAP treatment[11]. The increase in the levels of FGF21 preceded the detectable elevation in the levels of alanine transaminase (ALT) and aspartate aminotransferase (AST)[11]. Li et al. reported that during the reperfusion phase of hepatic ischaemia-reperfusion injury in mice, hepatic stellate cells secreted FGF10 to prevent early-stage hepatocellular apoptosis[12]. The expression of FGF7 increased in $Thy1^+$ mesenchymal cells, concurring with the response of the liver progenitor cell niche in mouse models of liver injury, as well as in the serum of patients with acute liver failure[13]. These findings suggested that FGFs function as stress-responsive factors that protect against liver injuries of various aetiologies. Our team previously identified FGF4 as a protective factor for non-alcoholic fatty liver disease (NAFLD)/non-alcoholic steatohepatitis (NASH), demonstrating anti-inflammatory, anti-apoptosis, and glucose- and lipid-lowering effects[14]. However, the role of FGF4 in ILI remains unclear.

In this study, we identified FGF4 as a responsive factor to liver damage caused by autoimmune hepatitis (AIH) and concanavalin A (ConA)- or S-100-induced ILI in both patients and mouse models. We found that loss of hepatic FGF4 exacerbated hepatocellular apoptosis and intrahepatic immune imbalance under ILI conditions. Conversely, pharmacological administration of recombinant FGF4 (rFGF4) inhibited apoptosis and corrected the immune imbalance. Mechanistically, FGF4 protected the liver from ILI by activating the FGFR4-Ca^{2+}/calmodulin-dependent protein kinase 2 (CaMKKβ)-phosphatase and tensin homologue (PTEN)-induced putative kinase 1 (PINK1) signalling axis, leading to the phosphorylation of mitochondrial B-cell lymphoma 2 (Bcl-2)-like protein 1-isoform L (Bcl-X_L) and inhibition of intrinsic apoptosis. Therefore, our study unravelled a previously unknown role of FGF4 in ILI, shedding new light on potential therapeutic strategies for treating immune disorder-associated liver injury in the clinic.

2. Materials and methods

2.1. Human liver samples

Paraffin-embedded human liver tissue samples were obtained from the Department of Pathology at the First Affiliated Hospital of Wenzhou Medical University (Wenzhou, China). The collection of patient samples was approved by the Ethics Committee of the First Affiliated Hospital of Wenzhou Medical University and conducted in accordance with the Declaration of Helsinki on Ethical Principles for Medical Research Involving Human Subjects (Ethical code (2021) No. 057). The diagnosis of AIH in liver biopsies from patients without other known chronic liver disease(s) was based on the International Autoimmune Hepatitis Group scoring system. None of the patients with AIH were on AIH therapy or taking drugs that might affect liver function at the time of their biopsies. Patients were divided into mild (men, $n = 3$; women, $n = 11$) and severe (men, $n = 6$; women, $n = 15$) groups according to the following three criteria[15]: (a) whether the serum level of transaminase was more than three-fold the upper limit of normal (ULN), (b) whether the level of immunoglobulin (Ig) G was greater than or equal to 1.5 ULN, and (c) moderate to severe interfacial hepatitis in the liver biopsy. The control group comprised normal paratumoural liver tissues from patients with hepatic haemangioma (men, $n = 3$; women, $n = 7$), with a similar men-to-women ratio. Details on patient information are listed in Supporting Information Table S1.

2.2. Animal study

Hepatocyte-specific *Fgf4* knockout (*Fgf4-LKO*) or *CaMKKβ* knockout (*CaMKKβ-KO*) mice were bred and genotyped as previously described[14]. The primers used for genotyping are listed in Supporting Information Table S2. Male C57BL/6 N mice were purchased from Charles River Animal Technology Co. Ltd. (Beijing, China). Male mice were used for all *in vivo* experiments. Animal care and all experimental procedures were approved by the Institutional Animal Care and Use Committee of Wenzhou Medical University, China (ethical code: WYYY-AEC-2021-294). Mice were housed at the Wenzhou Medical University in a controlled environment (23 ± 2 °C, 50%−60% humidity, 12 h light/dark cycle) under pathogen-free conditions, with free access to food and water.

2.3. ConA-induced ILI model and rFGF4 administration

To induce ILI in mice, 15 mg/kg ConA (C2010, Sigma−Aldrich, St. Louis, MO, USA) was administered *via* tail vein injection. In the rFGF4-treated group, mice were injected intraperitoneally with rFGF4 (1.0, 1.5, or 2.0 mg/kg body weight) or phosphate-buffered saline (PBS) (P1020, Solarbio, Beijing, China) as a carrier and control at 0 and 6 h after ConA treatment. The N-terminally truncated human FGF4 (Ala67-Leu206) was expressed and purified according to published protocols[14,16]. Mice were euthanized 18 h after the rFGF4 injection.

2.4. S-100-induced ILI model and rFGF4 administration

To isolate S-100, livers of C57BL/6 N male mice were excised under sterile conditions and minced into small pieces on ice. After washing with PBS, the liver pieces were lysed with RIPA lysis buffer (AR0101; Boster, Wuhan, China) and the homogenates were centrifuged at 150×*g* for 10 min. The supernatant was collected and centrifuged at 100,000×*g* for 1 h. To obtain liver-specific lipoprotein S-100, a 90 cm CL-6B Sepharose® column (Pharmacia, Uppsala, Sweden) on an AKTA Pure chromatography system (GE Healthcare, Chicago, IL, USA) was used, and the first peak was collected. To construct the ILI model, mice were administered 0.5 mL of 0.5−2.0 g/L fully emulsified S-100 in an equal volume of Complete Freund's Adjuvant (CFA) (Solarbio, Beijing, China) on Days 0 and 7 by intraperitoneal injection; the control group was injected with the same amount of PBS and CFA. On Day 28 after the S-100 injection, rFGF4 (1.5 mg/kg body weight) or an equal volume of PBS was intraperitoneally injected every other day for 2 weeks.

2.5. Enzyme-linked immunosorbent assay

The serum levels of alanine aminotransferase (C009-2-1), aspartate aminotransferase (C010-2-1) and IgG (H106-1-1) were measured using the respective kits according to the manufacturer's instructions (Nanjing Jiancheng Bioengineering Institute, Nanjing, China). The serum levels of interleukin (IL)-1β (SEA563Mu), IL-6 (SEA079Mu), interferon (IFN)-γ (SEA049Mu), tumour necrosis factor (TNF)-α (SEA049Mu), human-derived FGF4 (hFGF4) (SEA034Hu), and murine-derived FGF4 (mFGF4) (SEA034Mu) were determined using enzyme-linked immunosorbent assay kits according to the manufacturer's instructions (Cloud-Clone Corp, Wuhan, China).

2.6. Adeno-associated virus serotype 8-mediated gene transfer

Liver-specific *Fgfr4* and *Pink1* knock-downs were performed using adeno-associated viruses (AAVs). Constructs for porcine adenovirus (pAV)-thyroxine-binding globulin (TBG) promoter mediated expression of FGFR4 (AAV8-FGFR4) and pAV-TBG-PINK1 (AAV8-PINK1) shRNAs were synthesised by Vigene Biosciences (Shandong, China). All shRNA sequences are presented in Supporting Information Table S3. Briefly, AAV8-FGFR4, AAV8-PINK1, or control shRNA was injected once into 4-week-old wild-type (WT) male C57BL/6 N mice at a dose of 5×10^{11} vg/mouse *via* the tail vein. Samples were collected four weeks later.

2.7. FGF4 RNA-scope

The levels of *Fgf4* mRNA were measured using an RNA-scope assay (Bio-Techne Corporation, Minneapolis, MN, USA) according to the manufacturer's instructions. Briefly, liver sections were de-paraffinized and treated with H_2O_2 for 10 min at 26 °C to expose the RNA. After washing in PBS, the sections were immersed in the Target Reagent solution for 30 min and then incubated with Protease Plus at 40 °C for 30 min. After washing, the liver sections were incubated with human *Fgf4* (512291; Bio-Techne Corporation) or a mouse *Fgf4* probe (514311; Bio-Techne Corporation) for 2 h at 40 °C and then reacted with the Amp1-6 reagent and RED working solution. Fluorescence was visualised and photographed using a Nikon C2si confocal microscope (Nikon Corporation, Tokyo, Japan).

2.8. Histological analysis

Hematoxylin & Eosin (H&E) staining was performed on liver tissues with the kit according to the manufacturer's instructions (C0105S; Beyotime, China). Histological images of the liver sections were obtained under a light microscope (Nikon Eclipse Ni, Nikon Corporation) and analysed using the ImageJ software.

2.9. Immunohistochemical staining

The liver sections were baked at 65 °C for 5 h, followed by de-paraffinization with xylene and rehydration with a series of ethanol solutions of decreasing concentrations. The sections were then washed with PBS and boiled in 10 mmol/L of sodium citrate buffer (pH 6.0) at 100 °C for 2 min. After washing twice with PBS, the sections were treated with 3% H_2O_2 for 30 min and blocked with 5% bovine serum albumin (BSA) solution for 1 h. The sections were then incubated with primary antibodies against antigens (Table S4) overnight at 4 °C. Following a PBS wash, the sections were incubated with horseradish peroxidase (HRP)-conjugated goat anti-rabbit secondary antibody (11-035-003; Jackson ImmunoResearch Labs, West Grove, PA, USA) for 1 h at 25 °C and developed using a 3,3′-diaminobenzidine (DAB) kit (ZLI-9018; ZSGB-BIO, Beijing, China). Images were captured under an optical microscope (Olympus, Tokyo, Japan). Analysis and quantification were performed using the ImageJ software.

2.10. Immunofluorescence staining

Following antigen retrieval, the de-paraffinized or frozen liver sections were rinsed with PBS twice, blocked with 5% BSA for

1 h at 25 °C, and then incubated with primary antibodies against antigens (Supporting Information Table S4) overnight at 4 °C. The sections were then washed thrice with PBS and incubated with fluorescence-conjugated secondary antibodies (Table S4) for 1 h. The nuclei were counterstained with 4′,6-diamidino-2-phenylindole (DAPI) (ZLI-9018; ZSGB-BIO). Fluorescent images were captured under a Nikon C2si confocal microscope and analysed using the ImageJ software.

2.11. RNA extraction, cDNA synthesis, and qRT-PCR

Total RNA was extracted from liver tissues, sorted hepatocytes, and various immune cells using the RNeasy® Mini Kit (74106; Qiagen, Venlo, Netherlands) according to the manufacturer's instructions and then reverse-transcribed into cDNA using a PrimeScript™ RT Master Mix (RR036A; Takara, Kyoto, Japan) or SMARTScribe™ Reverse Transcriptase (639538; Takara). qRT-PCR was performed using TB Green® Premix Ex Taq™ II (RR820A; Takara) and respective primers (listed in Table S5) on a 7500 Real-Time PCR Detection System (Thermo Fisher Scientific, Inc., Waltham, MA, USA). The levels of mRNAs were determined using the $2^{-\Delta\Delta Ct}$ method and expressed as the ratio of the level of expression of the target gene to that of the housekeeping gene *β-actin*.

2.12. TUNEL staining

Paraffin-embedded liver sections were de-paraffinized and stained using the DeadEnd™ Fluorometric TUNEL System TB235 kit (G3250, Promega, Madison, WI, USA) according to the manufacturer's instructions. Stained liver tissue sections were visualised under a Nikon C2si confocal microscope.

2.13. Isolation of hepatocytes and mononuclear cells (MNCs)

Mouse liver was infused with HBSS and D-HBSS (without calcium) (H1025; Solarbio) pre-heated to 37 °C through the inferior vena cava. After opening the liver capsule, the cell suspension was filtered through a 100 μm cell strainer (352360; Corning, NY, USA) and then centrifuged at 50×*g* for 3 min to precipitate the hepatic parenchymal cells. To separate MNCs, the supernatant was centrifuged using a density gradient of 35% Percoll solution (65455-52-9; Solarbio) at 500×*g* for 15 min. Interphase cells were collected and lysed with 2−3 mL RBC lysis buffer (R1010; Solarbio) at 25 °C for 5−10 min, neutralised with 10 mL 1640 medium (10491; Solarbio), and then centrifuged at 300×*g* for 5 min at 4 °C. Lymphocytes were obtained after washing once with PBS. For immune cell sorting, CD45 MicroBeads (130-052-301; Miltenyi Biotech, Bergisch Gladbach, Germany) were added to the suspension of hepatic MNCs. The LS column (130-042-401; Miltenyi Biotech) was placed into the QuadroMACS™ Separator (130-091-051; Miltenyi Biotech), and the cell suspension was added to the separator to collect $CD45^+$ cells, according to the manufacturer's instructions.

2.14. Flow cytometry

The isolated hepatic MNCs were incubated with anti-mouse CD16/32 antibody (156603; BioLegend, San Diego, CA, USA) for 10 min to prevent non-specific binding, and then stained with antibodies against the cell-surface markers lymphocyte antigen 6 complex locus G6D (Ly6G), CD45, CD3, NK1.1, CD4, CD11b, F4/80, CD206, MHCII, and TCR-*β* at 4 °C for 30 min[17]. Dead cells were excluded using the Zombie NIR Fixable Viability Kit (423105; BioLegend). To analyse the levels of apoptosis and mitochondrial permeability transition pore (mPTP) opening, hepatic parenchymal cells were stained using the Allophycocyanin Annexin V/7-Amino-Actinomycin D (7-AAD) Apoptosis Detection Kit (640930; BioLegend) or Calcein AM mPTP detection kit (C2012; Beyotime) according to the manufacturer's instructions. The details of the labelling scheme are listed in Table S4.

2.15. T-cell proliferation in vitro

Purified T-cells were labelled using the CFSE Cell Division Tracker Kit (423801; Biolegend) according to the manufacturer's instructions. Cell density was adjusted to 2×10^6/mL and cells were stimulated with 2.5 μg/mL ConA. After 24 h, 1.0 μg/mL rFGF4 or an equal volume of PBS was added to cells and incubated for another 72 h. T-cells were incubated with the anti-mouse CD16/32 antibody (156603; BioLegend) for 10 min, and then stained using the Zombie NIR Fixable Viability Kit (423105; BioLegend) and antibodies against the cell-surface markers CD3, CD4, and CD69. The details of the labelling scheme are listed in Table S4.

2.16. $[Ca^{2+}]$ and cytochrome (Cyt) C concentrations in mitochondria and cytoplasm

Mitochondria were isolated from freshly prepared hepatic parenchymal cells using a mitochondrial isolation kit (C3606; Beyotime), according to the manufacturer's instructions. Mitochondrial and cytoplasmic protein concentrations were determined using a Pierce bicinchoninic acid protein assay kit (Pierce Biotechnology, Rockford, IL, USA). Changes in the flux of calcium ions ($[Ca^{2+}]$; C004-2-1; Nanjing Jiancheng Bioengineering Institute) and Cyt *C* (H190; Nanjing Jiancheng Bioengineering Institute) between the mitochondria and cytoplasm were measured according to the manufacturer's instructions.

2.17. Western blot analysis

Liver tissues, hepatic parenchymal cells, and mitochondria were homogenised in corresponding lysis buffers (AR0101, AR0103, AR0156; Boster). Cell and tissue lysates were mixed with sodium dodecyl sulphate (SDS) sample buffer, boiled, and separated by 8%−15% SDS-polyacrylamide gel electrophoresis (PAGE), followed by electrophoretic transfer onto a nitrocellulose membrane (Millipore, MA, USA). Immunoblotting was performed using the primary antibodies listed in Table S4. Images were captured using an Amersham Imager680 and analysed using the ImageJ software with glyceraldehyde-3-phosphate dehydrogenase (GAPDH) or Cyt *C* oxidase subunit 4 (COXIV) used as an internal reference.

2.18. Co-immunoprecipitation assays

HEK293 cells (Cell Biolabs, Inc., Chicago, IL, USA) were lysed in immunoprecipitation (ip) buffer (20 mmol/L Hepes, 120 mmol/L NaCl, 1% Triton-X100) containing protease and phosphatase inhibitors (Thermo Fisher Scientific). IP was performed by incubating 500 mg of whole-cell lysates (INPUT) with the indicated antibodies (listed in Table S4) for 12 h at 4 °C. Mouse or rabbit IgG were used as controls for non-specific co-immunoprecipitation. The following day, protein A- or G- beads (Sigma−Aldrich, St. Louis., MO, USA) were added to lysates and incubated for 6 h

at 4 °C. The immuno-complexes were then washed thrice with lysis buffer, re-suspended in SDS sample buffer (Life Technologies, Frederick, MD, USA), and processed for Western blotting.

2.19. RNA sequencing (RNA-seq) analysis

Total RNA was extracted, and a genome-wide transcriptomic analysis was conducted (LCBIOTECHNOLOGIS (HANGZHOU) CO., LTD., Zhejiang, China). Differentially expressed mRNAs with a *P*-value <0.05 were selected using the R package edgeR (https://bioconductor.org/packages/release/bioc/html/edgeR.html) or DESeq2 (http://www.bioconductor.org/packages/release/bioc/html/DESeq2.html). A pathway with a *P*-value <0.05, normalised enrichment score (NES) > 1, and false discovery rate (FDR) < 0.25 was defined as a significantly enriched pathway.

2.20. Statistical analysis

Data were analysed using GraphPad Prism 8 and presented as the mean ± standard error of mean (SEM). For experiments with only two groups, the two-tailed Student's *t*-test or Mann−Whitney U test was used for statistical comparisons. Ordinary one-way or two-way analysis of variance (ANOVA) with *post-hoc* tests (Tukey or Sidak) were used to compare data between multiple groups, as indicated in Figure legends.

2.21. Ethics declarations

The collection of patient samples was approved by the ethics committee of The First Affiliated Hospital of Wenzhou Medical University and conducted in accordance with the Declaration of Helsinki on Ethical Principles for Medical Research Involving Human Subjects (Ethical code (2021) No. 057). All animal care and experimental procedures were approved by the Institutional Animal Care and Use Committee of Wenzhou Medical University, China (ethical code: WYYY-AEC-2021-294).

3. Results

3.1. Levels of hepatic FGF4 coincide with early pathogenesis of ILI

Autoimmune hepatitis is a representative form of ILI with unclear aetiology[3,8]. We found that the levels of serum ALT and AST in patients in the severe group were notably higher than those in the mild and control groups (Fig. 1A and B and Table S1). RNA-scope and immunohistochemistry analyses revealed that the levels of both the hepatic FGF4 mRNA and protein were increased in patients with mild liver injury but substantially decreased in those having severe liver damage, even falling below the levels observed in livers from healthy individuals (Fig. 1C−E).

Concanavalin A is known to directly induce the proliferation of T-cells and immune responses, leading to intrahepatic infiltration and expansion of T-cells and macrophages and subsequent liver injury[18]. As a hepatic autoantigen, exogenous S-100 in excessive amounts is known to induce antigen-triggered antibody immune responses and chronic liver injury[19]. In the ConA-induced acute ILI mouse model, we noticed the markedly occurrence of focal hepatocyte deaths associated with prominent lymphocytic infiltration and increased levels of transaminases at 18 h after the ConA injection, followed by a recovery phase within three days (Fig. 1F and G). Notably, the changes in both the mRNA and protein levels of hepatic FGF4 followed a biphasic pattern similar to the pathological progression of ILI (Fig. 1H−L). In the S-100-induced chronic ILI model, both the mRNA and protein levels of hepatic FGF4 were progressively and markedly increased at Day 28, followed by returning to below the basal levels at Day 42, during which the increasing trend of S-100-induced focal immune cell infiltration and transaminase levels continued (Fig. 1M−P).

We also determined the expression levels of endogenous FGF4 in hepatocytes and the number of major intrahepatic immune cells using markers of NK1.1 for natural killer (NK) cells, CD3 for T-cells, and F4/80 for macrophages. Consistent with our previously reported results[14], FGF4 was specifically co-expressed in ALB^+ hepatocytes in both patients with AIH and hepatic haemangioma (HH) as control. We found that the levels of FGF4 were increased in patients with mild liver injury but decreased in those with severe liver injury, as indicated by fluorescence intensity (Supporting Information Fig. S1A and B). Similarly, in the ConA-induced ILI mouse model, FGF4 was expressed in ALB^+ hepatocytes (Supporting Information Fig. S1C−D) without co-localisation with NK1.1, CD3, or F4/80, and was significantly increased 18 h after ConA injection (Fig. S1E). Following cell sorting, we observed that the mRNA levels of *Fgf4* were significantly increased in hepatocytes under the disease state, whereas its levels in $CD3^-NK1.1^+$ NK cells, $CD3^+NK1.1^-$ T-cells, or $F4/80^+CD11b^+$ macrophages were not significantly different compared to the control group (Fig. S1F−H). To understand the transcriptional mechanism for controlling the adaptive changes in the levels of hepatic FGF4, we conducted RNA-seq analysis of liver tissues from the control and ConA-induced ILI mice. Our data showed that the expression levels of *Ppar-α*[20], *Nur77*[21,22], *Atf3*[23], *Atf4*[24], and *Hnf6*[25], which have been reported to transcriptionally regulate the expression of FGFs, were significantly increased in response to ConA treatment (Fig. S1I). Furthermore, we analysed the intrahepatic expression of these genes in mice with ConA- and S-100-induced ILI. We found that the mRNA levels of hepatic *Nur77* and *Atf3* consistently demonstrated a bidirectional pattern in both ILI models, recapitulating the expression pattern of hepatic *Fgf4* throughout the progression of the disease (Fig. S1J and K). Thus, all the data from patients with AIH and both the acute and chronic ILI mouse models suggested that the expression of FGF4 in hepatocytes is an early response to liver injury during ILI pathogenesis.

3.2. Hepatocyte-specific deletion of Fgf4 exacerbates ConA- and S-100-induced liver damage

To understand the role of endogenous FGF4 in ILI, we generated a mouse model with hepatocyte-specific deletion of *Fgf4* (*Fgf4*$^{-/-}$ or *Fgf4-LKO*). In normal unstressed conditions, the hepatic FGF4 deficiency appeared to have minimal effects on the liver morphology, histology, or overall body parameters (Fig. 2A). However, *Fgf4*$^{-/-}$ mice are sensitive to both acute ConA and chronic S-100 challenges, which induce experimental ILI inflammation and damage[18,19]. Examination of the H&E-stained sections revealed more prominent lymphocytic infiltration into the peri-central vein area and hepatic lobule as well as broader areas of swelling and death of hepatocytes in *Fgf4*$^{-/-}$ ILI mice than in *Fgf4*-floxed control mice under ConA insult or saline treatment (control) (Fig. 2A). *Fgf4* deletion led to a further increase in the serum levels of ALT and AST under ConA insult (Fig. 2B and C). We also found that the serum levels of pro-inflammatory cytokines, including IL-1β, IL-6, IFN-γ, and TNF-α were also increased (Fig. 2D), indicating that FGF4 deficiency exacerbated the ConA-induced hepatic inflammatory response. In addition, the

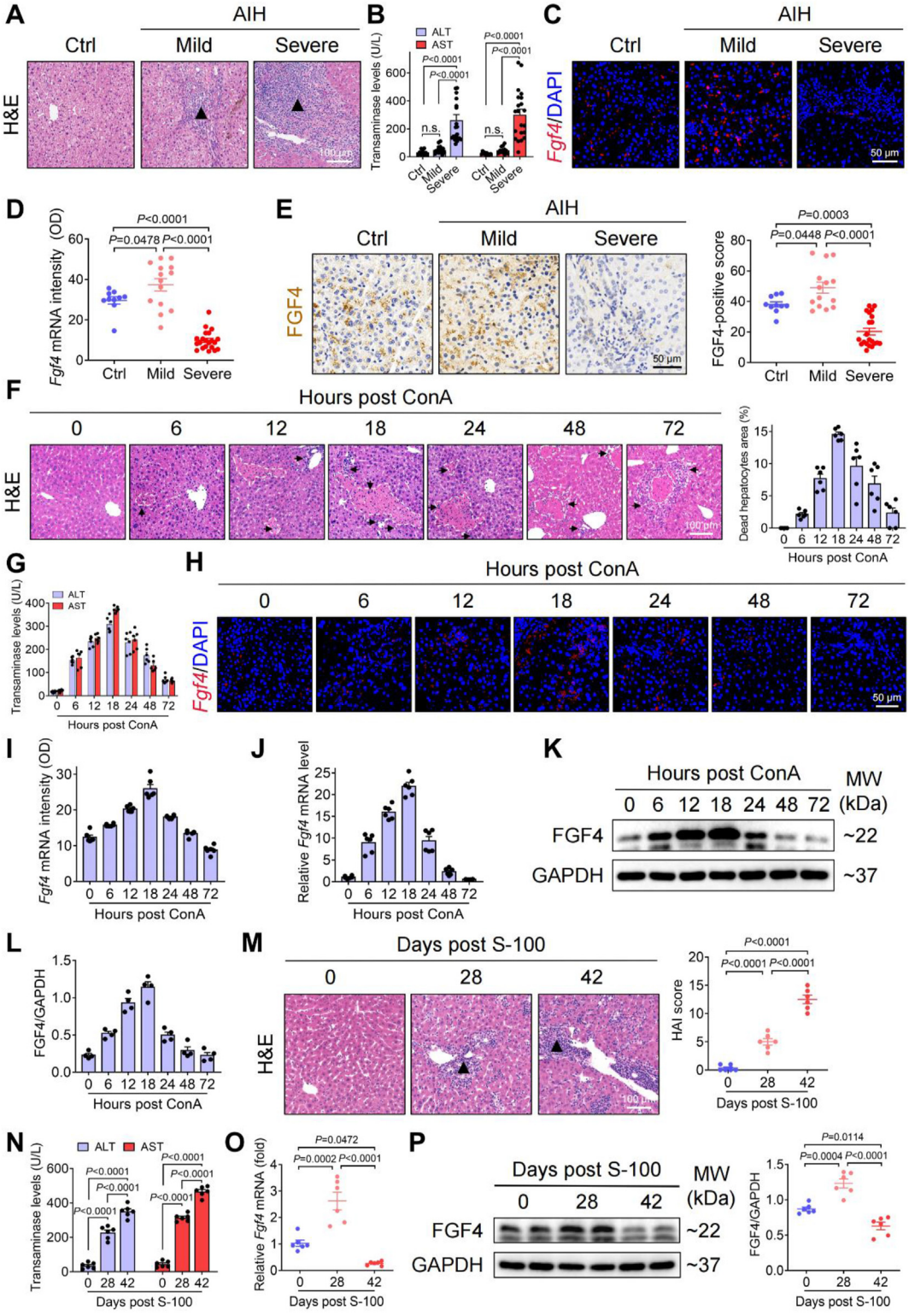

Figure 1 Intrahepatic FGF4 levels are associated with ILI pathogenesis. (A) Representative H&E staining images of human liver sections from patients with AIH and hepatic hemangioma. The areas infiltrated by lymphocytes are indicated by black triangles. Scale bar = 100 μm. (B) Serum levels of ALT and AST in the indicated groups. (C, D) Analyses of the mRNA levels of *Fgf4* in human liver sections from the indicated groups using RNA scope. (E) Representative IHC images and quantification of FGF4 immunostaining in human liver sections from the indicated groups. Scale bar = 50 μm. (F) Representative H&E-stained images and statistical analysis (%) of focal hepatocyte death in liver tissues of mice treated with ConA for 0, 6, 12, 18, 24, 48, and 72 h. The area of dead hepatocytes is circled by broken white trace lines. Lymphocytes are indicated by black arrows. Scale bar = 100 μm. (G) Serum levels of ALT and AST in the indicated mice. (H, I) Analysis of the mRNA levels of *Fgf4* in liver tissues from the indicated mice using RNA scope. Scale bar = 50 μm. (J) Relative mRNA levels of *Fgf4* in liver tissues from the indicated mice as

loss of *Fgf4* resulted in a significant increase in the ConA-induced intrahepatic infiltration of $CD4^+$ T-cells (Fig. 2E).

Similarly, in mice with chronic S-100-induced ILI, we observed that FGF4 deficiency exacerbated liver damage, leading to a 64.15% increase in the histology activity index (HAI) score (Fig. 2F). Serum levels of AST and ALT (Fig. 2G) and the representative pro-inflammatory cytokines IL-1β, IL-6, IFN-γ, and TNF-α were all significantly increased (Fig. 2H). Different from the acute ConA effect at 18 h, chronic S-100 (42 d) induced a significant increase in the serum levels of IgG, which was further aggravated by FGF4 depletion (Fig. 2I). Moreover, FGF4 deficiency also resulted in a significant increase in the S-100-induced intrahepatic infiltration of $CD4^+$ T-cells (Fig. 2J). Thus, our data obtained from the mouse models of both ConA- and S-100-induced ILI revealed that hepatic FGF4 deficiency exacerbated immune-mediated liver inflammation and injury, suggesting a possible protective role of FGF4 against both acute and chronic ILI.

3.3. *Administration of recombinant FGF4 ameliorates ConA- and S-100-induced liver injury*

To better understand the pathophysiological role of FGF4 in ILI, we administered structurally modified, non-mitogenic recombinant FGF4 (rFGF4)[14,16] intraperitoneally (ip) into mice at doses of 1.0, 1.5, and 2.0 mg/kg body weight at the start and 6 h after the ConA challenge (Fig. 3A). We observed that at 18 h post-injection, the rFGF4 treatment caused a dose-dependent reduction in focal areas of hepatocyte death, as observed through histological examination of liver sections (Fig. 3B). Concomitantly, the serum levels of ALT and AST were notably reduced by rFGF4 treatment at both doses of 1.5 and 2.0 mg/kg (Fig. 3C); this was accompanied by marked decreases in the levels of serum pro-inflammatory cytokines IL-1β, IL-6, IFN-γ, and TNF-α (Fig. 3D), and inhibition of ConA-induced intrahepatic infiltration of $CD4^+$ T cells compared with those in the saline control (Fig. 3E). Moreover, rFGF4 supplementation also significantly improved liver histopathological damage (Supporting Information Fig. S2A and B) and reduced the levels of serum inflammatory factors and ConA-induced hepatic infiltration of $F4/80^+$ cells in the *Fgf4-LKO* mice (Fig. S2C and D).

We observed similar beneficial effects of rFGF4 supplementation in mice with S-100-induced chronic ILI. Treatment with rFGF4 at a dose of 1.5 mg/kg body weight every other day, starting from Day 28 for a duration of two weeks (Fig. 3F), effectively diminished areas of focal hepatic death and inflammatory cell infiltration and reduced the HAI score by 85.71% (Fig. 3G). The serum levels of transaminases (Fig. 3H), antibody IgG (Fig. 3I), pro-inflammatory cytokines IL-1β, IL-6, IFN-γ, and TNF-α (Fig. 3J), and intrahepatic infiltration of $CD4^+$ T-cells were all reduced as well (Fig. 3K). Similarly, rFGF4 replenishment also improved S-100-induced liver injury in *Fgf4-LKO* mice (Fig. S2E−I). Further, we observed that the fluctuations in the serum concentration of murine-derived FGF4 (mFGF4) (Supporting Information Fig. S3A) mirrored the changes in the expression levels of intrahepatic FGF4 during the S-100-induced injury (Fig. 1O and P). In contrast, the serum concentrations of human-derived rFGF4 continued to rise as the duration of rFGF4 administration extended, and were sustained at a high level (Fig. S3A). This suggests that the observed protective effect following rFGF4 administration is attributed to the elevated levels of exogeneous rFGF4, not endogenous mFGF4. In line with the findings of our previous study that the N-terminal truncation of FGF4 diminishes its mitogenic potency[14,16], levels of hepatocyte proliferation-related markers, such as Ki67 and PCNA, did not change or were even significantly reduced relative to the model group following long-term administration of rFGF4 (Fig. S3B and C), suggesting the involvement of other cellular mechanisms in the protection from ILI-induced liver damage.

3.4. *rFGF4 targets hepatocellular FGFR4 to protect the liver from ILI-induced damage*

We have previously demonstrated that rFGF4 acts on hepatocellular FGFR4, resulting in the amelioration of NASH[14]. To ascertain whether the protective effect of rFGF4 against ILI-associated liver damage is also mediated by hepatocellular FGFR4, we examined the changes in the mRNA levels of *Fgfrs* under these conditions. Under normal physiological conditions, *Fgfrs*, predominantly *Fgfr4*, were expressed in hepatocytes, with macrophages exhibiting low levels of *Fgfr1* and *Fgfr2*, and T-cells expressing a small amount of *Fgfr1* (Fig. 4A). Compared with the control group, the levels of *Fgfr4* mRNA were significantly increased only in hepatocytes following ConA treatment (Fig. 4A). However, no significant changes were observed in the expression levels of all *Fgfrs* in sorted immune cells (Fig. 4A). Consistently, analysis of co-localisation of FGFR4 and albumin revealed an overlap of FGFR4 and albumin stains in both normal and diseased states and the fluorescence intensity of FGFR4 stains was significantly elevated following ConA treatment (Fig. 4B). Further, we constructed AAV8-TBG-mediated *Fgfr4* shRNA that specifically reduces *Fgfr4* in hepatocytes (Fig. 4C−E). We observed a significant attenuation of the protective effect of rFGF4 against ConA-induced liver pathological injury (Fig. 4F, G). This was accompanied by increases in the serum concentrations of inflammatory factors (Fig. 4H) and the intrahepatic infiltration of $F4/80^+$ macrophages (Fig. 4I) and $CD3^+CD4^+$ T-cells (Fig. 4J). Given that ILI is primarily caused by an abnormal T cell-mediated immune response, we further sorted intrahepatic T cells from normal wild-type mice, stimulated them with 2.5 μg/mL ConA *in vitro* for 24 h, and then treated them with 1.0 μg/mL rFGF4 for 72 h. The results showed that rFGF4 did not significantly affect T-cell proliferation (Supporting Information Fig. S4A) or CD69 expression levels (Fig. S4B). These results strongly suggests that the protective effects of rFGF4 on ILI are contingent upon the activation of

measured using qRT-PCR. (K, L) Western blot analysis of the expression of FGF4 in liver tissues from the indicated mice. Representative H&E-stained images (left) and HAI analysis (right) of liver sections from mice treated with S-100 for 0, 28, and 42 days. The areas infiltrated by lymphocytes are indicated by black triangles. Scale bar = 100 μm. Serum levels of ALT and AST in mice. Relative mRNA levels of *Fgf4* in liver tissues from the indicated mice measured by qRT-PCR. Western blot analysis of FGF4 in liver tissues from the indicated mice. (A−E) Control group: $n = 10$, mild group: $n = 14$, severe group: $n = 21$; (F, G, I, J, L−P) $n = 6$ per group. Data are the mean ± SEM. (B) Ordinary two-way analysis of variance (ANOVA) followed by Tukey's *post hoc* test; (D, E, M, O, P) Ordinary one-way ANOVA followed by Tukey's *post hoc* test. (N) Ordinary two-way ANOVA followed by Sidak *post hoc* test. n.s., not significant.

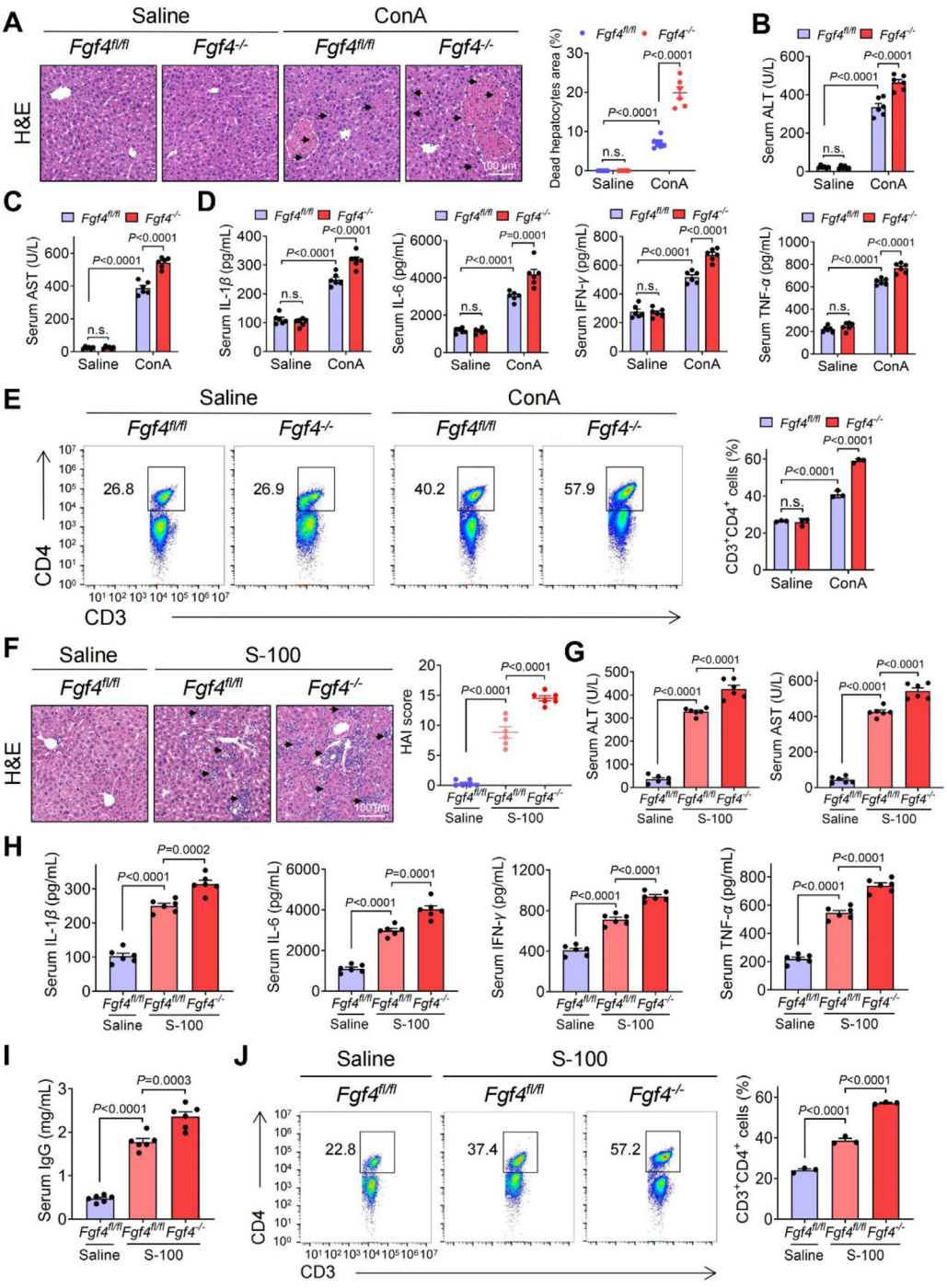

Figure 2 Hepatocyte-specific deletion of *Fgf4* exacerbates ConA- and S-100-induced liver damage. (A) Representative H&E-stained images (left) and statistical analysis (%) (right) of focal hepatocyte death in liver tissues from saline- or ConA-treated $Fgf4^{fl/fl}$ and $Fgf4^{-/-}$ mice. Areas of dead hepatocytes are circled with white dotted trace lines, and lymphocytes are indicated by black arrows. Scale bar = 100 μm. (B, C) Serum levels of ALT and AST in the indicated groups. (D) Serum levels of pro-inflammatory cytokines in the indicated groups. (E) Changes in the infiltration rate of $CD3^+CD4^+$ T-cells in the livers of the indicated groups. (F) Representative H&E-stained images (left) and HAI analysis (right) of liver tissues from saline- or S-100-treated $Fgf4^{fl/fl}$ and $Fgf4^{-/-}$ mice. Lymphocytes are indicated by black arrows. Scale bar = 100 μm. (G) Serum levels of ALT and AST in the indicated groups. (H) Serum levels of pro-inflammatory cytokines in the indicated groups. (I) Serum levels of IgG in the indicated groups. (J) Changes in the infiltration rate of $CD3^+CD4^+$ T-cells in the livers of the indicated groups. (A−D, F−I) $n = 6$ per group; (E, J) $n = 3$ per group. Data are the mean ± SEM. (A−E) Ordinary two-way ANOVA followed by Tukey's *post hoc* test. (F−J) Ordinary one-way ANOVA followed by Tukey's *post hoc* test. n.s., not significant.

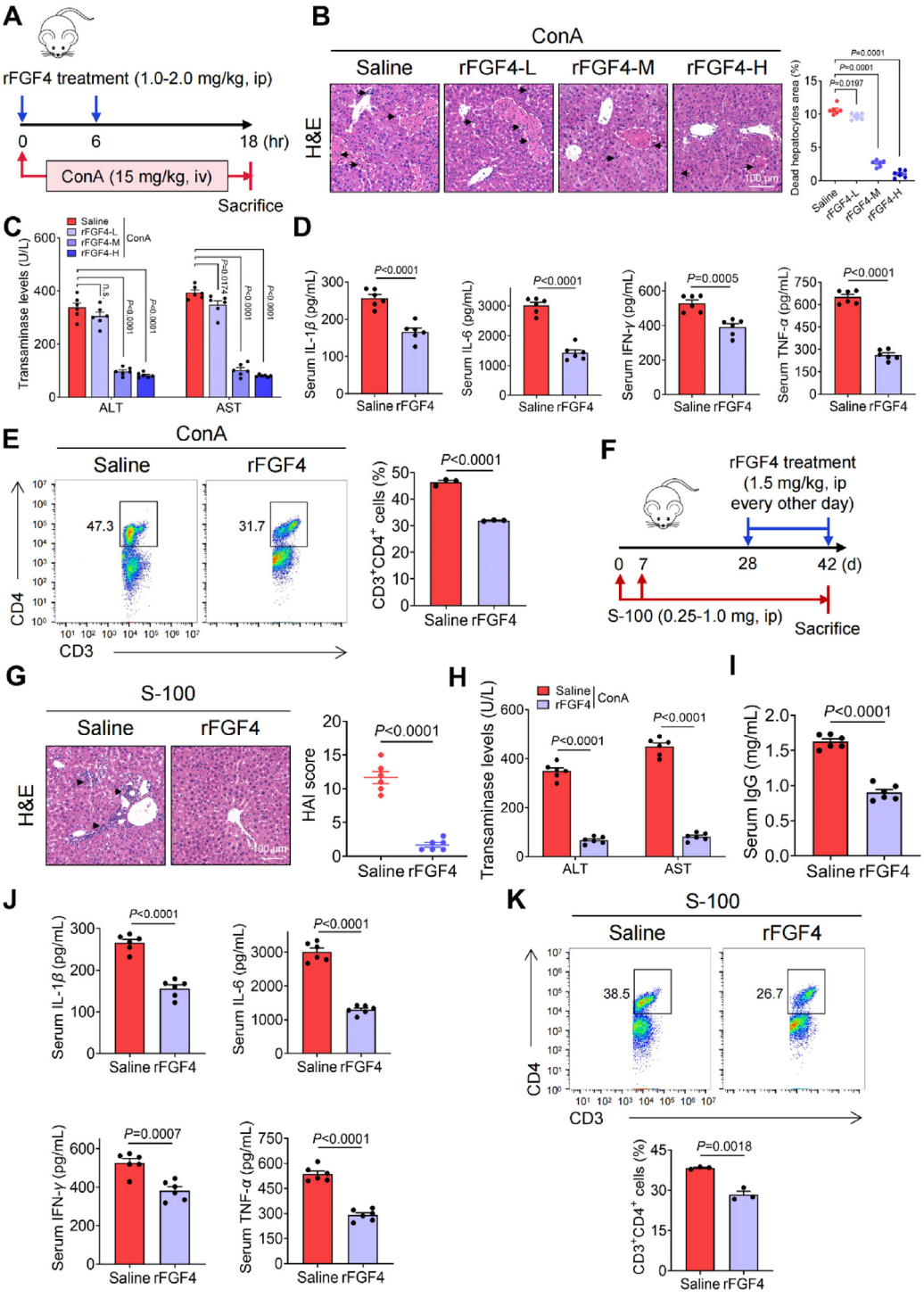

Figure 3 Administration of recombinant FGF4 ameliorates ConA- and S-100-induced liver damage. (A) Schematic of the rFGF4 treatment regimen for mice with ConA-induced ILI. (B) Representative H&E staining images (left) and statistical analysis (%) (right) of focal hepatocyte death in liver tissues of ConA-induced ILI groups following treatments with different concentrations (L: 1.0 mg/kg, M: 1.5 mg/kg, H: 2.0 mg/kg body weight) of rFGF4. Areas of dead hepatocytes are circled using white dotted trace lines, and lymphocytes are indicated by black arrows. Scale bar = 100 μm. (C) Serum levels of ALT and AST in the indicated groups. (D) Serum levels of pro-inflammatory cytokines in the indicated groups. (E) Changes in the infiltration rate of $CD3^+CD4^+$ T-cells in the livers of the indicated groups. (F) Schematic representation of the rFGF4 treatment regimen in mice with S-100-induced ILI. (G) Representative H&E-stained images (left) and HAI analysis (right) of liver tissues from S-100-treated mice after rFGF4 administration. Lymphocytes are indicated by black arrows. Scale bar = 100 μm. (H) Serum levels of ALT and AST in the indicated groups. (I) Serum levels of IgG in the indicated groups. (G) Serum levels of pro-inflammatory cytokines in the indicated groups. (K) Changes in the infiltration rate of $CD3^+CD4^+$ T-cells in the livers of the indicated groups. (B–D, G–J) $n = 6$ per group; (E, K) $n = 3$ per group. Data are the mean ± SEM. (B) Ordinary one-way ANOVA followed by Dunnett's *post hoc* test. (C, H) Ordinary two-way ANOVA followed by Sidak *post hoc* test. (D, E, G, I–K) Two-tailed unpaired Student's *t*-test. n.s., not significant.

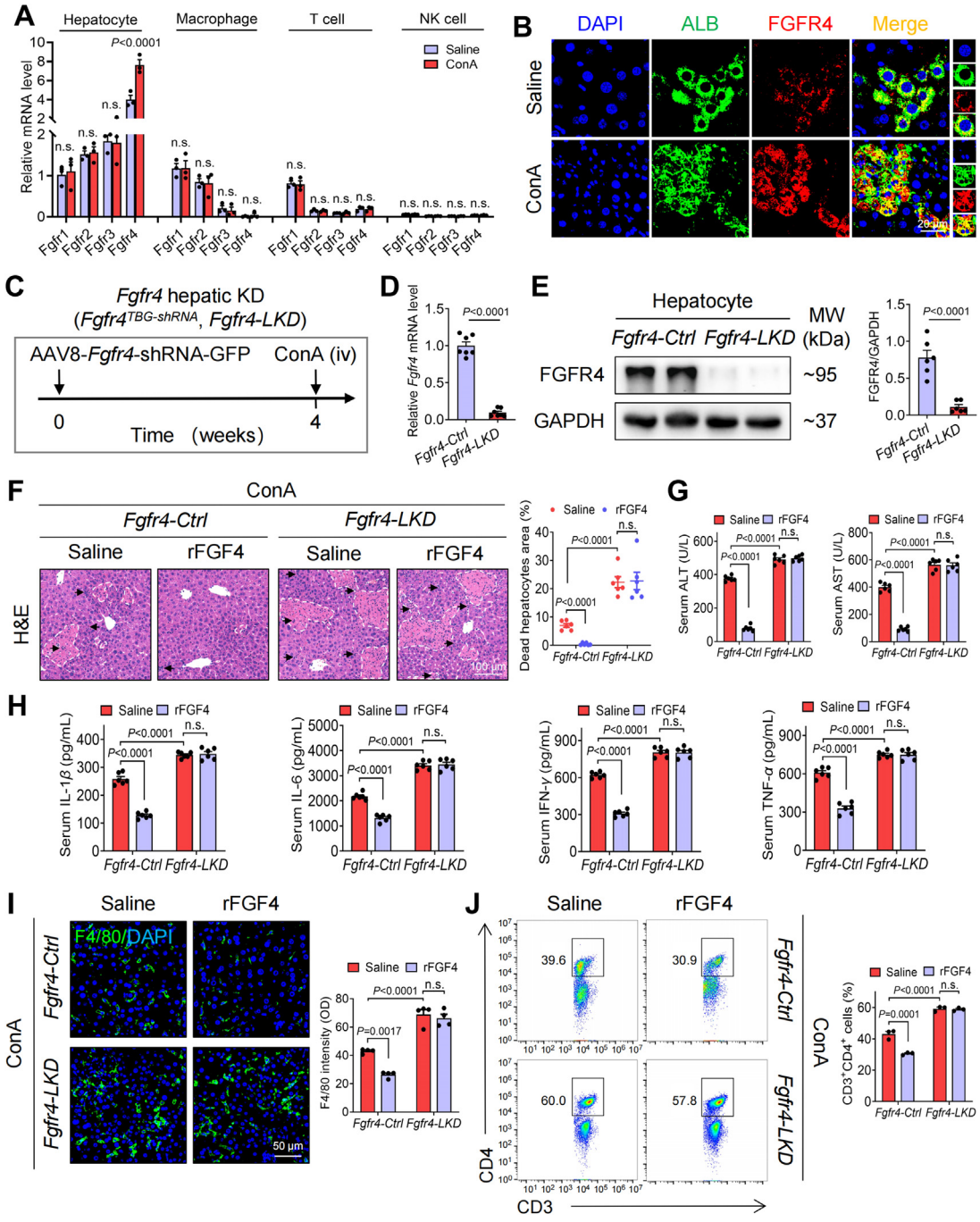

Figure 4 FGF4 targets hepatic FGFR4 to protect against ILI. (A) Relative mRNA levels of *Fgfr1–4* in the sorted hepatocytes, macrophages, T-cells, and NK cells from the saline or ConA-treated mice measured by qRT-PCR. (B) Co-localisation of FGFR4 expression (red) in hepatocytes with albumin (green) by immunofluorescence staining. Scale bar = 20 μm. (C) Schematic of experiment with hepatic knock-down of *Fgfr4* (*Fgfr4-LKD*) in mice. (D) Relative mRNA levels of *Fgfr4* in hepatocytes of *Fgfr4-LKD* and control mice measured by qRT-PCR. (E) Western blot analysis of FGFR4 in hepatocytes of *Fgfr4-LKD* and control mice. (F) Representative H&E-stained images and statistical analysis (%) of focal hepatocyte death in liver tissues from ConA- and rFGF4-treated *Fgfr4-Ctrl* and *Fgfr4-LKD* mice. Areas of dead hepatocytes are circled with white broken trace lines, and lymphocytes are indicated by black arrows. Scale bar = 100 μm. (G) Serum levels of ALT and AST in the indicated groups. (H) Serum levels of pro-inflammatory cytokines in the indicated groups. (I) Representative images and quantification of F4/80 (green) immunofluorescence staining with DAPI (blue) counterstaining in liver sections from the indicated groups. Scale bar = 50 μm. (J) Changes in the infiltration rates of $CD3^+CD4^+$ T-cells in the livers of the indicated groups. (A, J) $n = 3$ per group; (I) $n = 4$ per group; (D–H) $n = 6$ per group. Data are the mean ± SEM. (A) Ordinary one-way ANOVA followed by Sidak *post hoc* test. (D, E) Two-tailed unpaired Student's *t*-test. (F–J) Ordinary two-way ANOVA followed by Tukey's *post hoc* test. n.s., not significant.

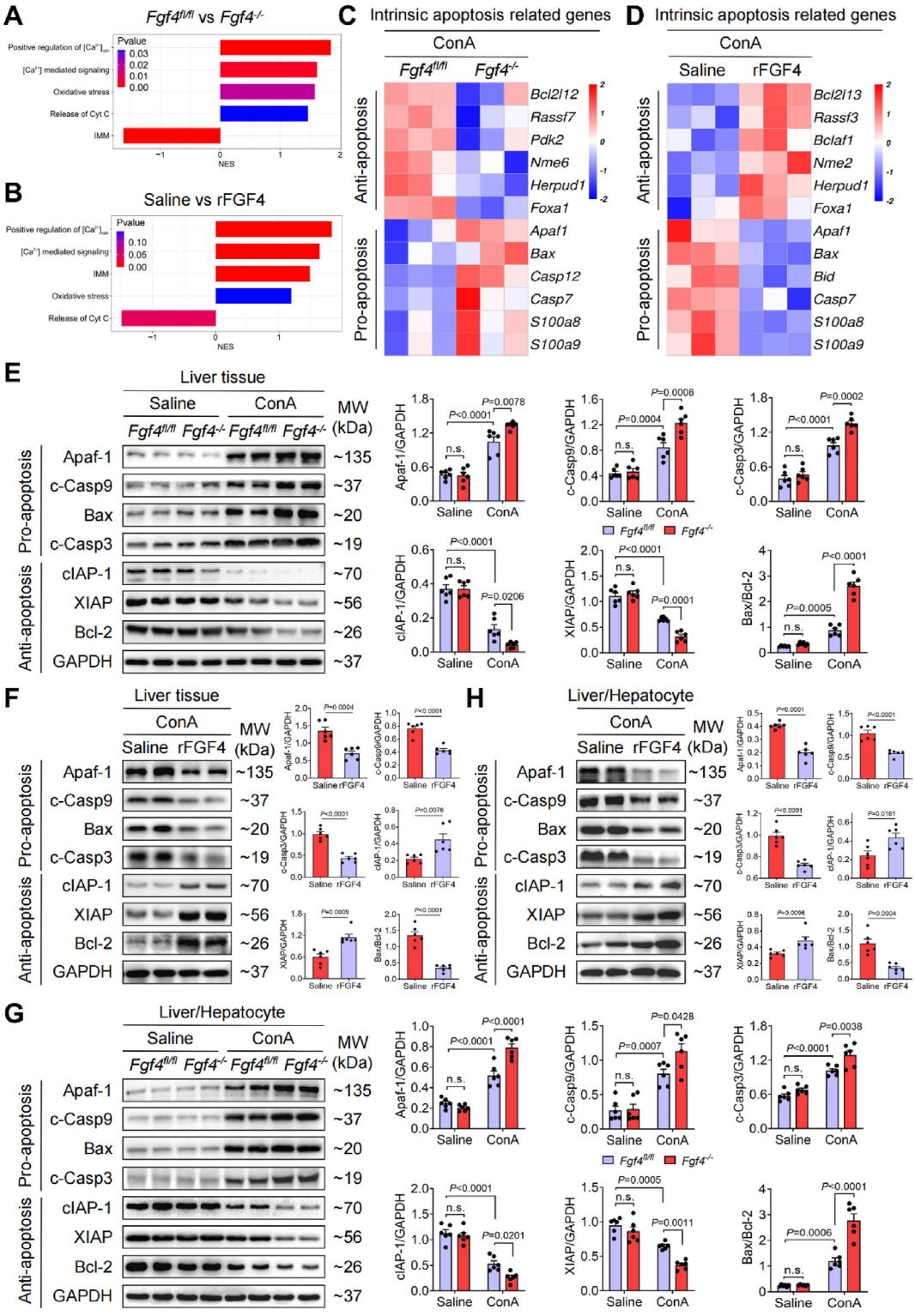

Figure 5 FGF4 inhibits intrinsic apoptosis caused by ConA treatment in mouse hepatocytes. (A) Normalised enrichment scores of intrinsic apoptosis-related pathways in liver tissues from ConA-treated $Fgf4^{fl/fl}$ and $Fgf4^{-/-}$ mice based on RNA-seq data. $n = 3$ per group. (B) Normalised enrichment scores of intrinsic apoptosis-related pathways in liver tissues of ConA- and rFGF4-treated mice based on RNA-seq data. (C) Heatmap of representative differentially expressed genes related to intrinsic apoptosis in liver tissues of ConA-treated $Fgf4^{fl/fl}$ and $Fgf4^{-/-}$ mice based on RNA-seq data. (D) Heatmap of representative and differentially expressed genes related to intrinsic apoptosis in liver tissues from ConA- and rFGF4-treated mice based on RNA-seq data. (E, F) Western blot analysis of proteins related to the intrinsic apoptotic pathway upon hepatic FGF4 deficiency or rFGF4 treatment in total liver lysates from the indicated groups. (G–H) Western blot analysis of proteins related to the intrinsic apoptotic pathway upon hepatic FGF4 deficiency or rFGF4 treatment in hepatocytes isolated from the indicated groups. (A–D) $n = 3$ per group; (E–H) $n = 6$ per group. Data are the mean ± SEM. (E, G) Ordinary two-way ANOVA followed by Tukey's *post hoc* test. (F, H) Two-tailed unpaired Student's *t*-test. n.s., not significant.

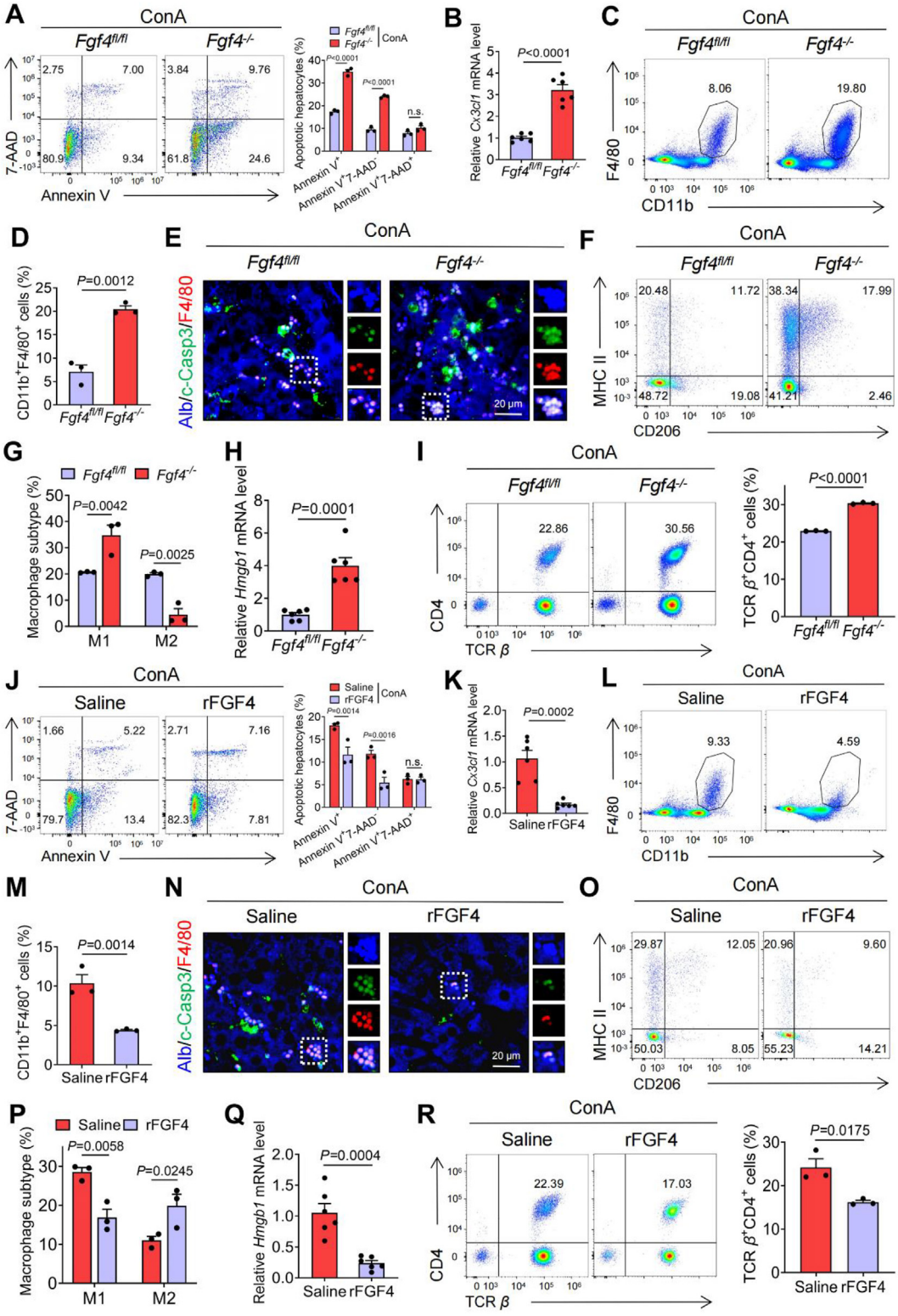

Figure 6 Hepatic FGF4 inhibits apoptosis-evoked macrophage and T-cell infiltration under ILI conditions. (A, J) Changes in the frequency of Annexin V^+ apoptotic hepatocytes isolated from the livers of the indicated groups. (B, K) Relative mRNA levels of *Cx3cl1* in total liver lysates from the indicated groups. (C, L) Representative FCM of $Ly6G^-CD45^+F4/80^+CD11b^+$ macrophage infiltration in livers of the indicated groups. (D, M) Changes in the infiltration of $Ly6G^-CD45^+F4/80^+CD11b^+$ macrophages in livers of the indicated groups. (E, N) Recruitment of macrophages to apoptotic hepatocytes as indicated by albumin (blue), c-Casp3 (green), and F4/80 (blue) immunofluorescent staining in liver tissues from the indicated groups. Scale bar = 20 μm. (F, O) Changes in the intrahepatic infiltration of the $Ly6G^-F4/80^+CD11b^+MHCII^+CD206^-$ M1-type and $Ly6G^-F4/80^+CD11b^+MHCII^-CD206^+$ M2-type macrophages of the indicated groups. (G, P) Relative mRNA levels of *Cx3cl1* in livers of the indicated groups. (H, Q) Relative mRNA levels of *Hmgb1* in liver lysates of the indicated groups.

hepatocellular FGFR4, rather than a direct action on immune cells.

3.5. FGF4 inhibits intrinsic apoptotic pathway in hepatocytes

Apoptosis is a well-known mechanism underlying hepatocellular death in ILI[5,6]. Our RNA-seq with gene set and pathway enrichment analyses revealed that both the deficiency of hepatic FGF4 (Supporting Information Fig. S5A and B) and treatment with rFGF4 (Fig. S5C and D) had profound yet contrasting effects on intrahepatic apoptotic pathways. Consistent with these findings, we observed a substantial increase in the number of cells undergoing apoptosis following ConA insult, as indicated by the intensity of terminal deoxynucleotidyl transferase-mediated nick-end labelling (TUNEL), in the livers of *Fgf4-LKO* ILI mice (Fig. S5E). Conversely, treatment with rFGF4 markedly decreased the rate of apoptosis (Fig. S5F). Furthermore, markers of intrinsic apoptosis associated with the perturbation of mitochondrial function, including cytoplasmic Ca^{2+} concentration ($[Ca^{2+}]_{cyt}$), Ca^{2+} signalling pathway, level of oxidative stress, Cyt *C* release, and mitochondrial membrane potential[26,27], were all significantly affected by both hepatic FGF4 deficiency (Fig. 5A) and exogenous FGF4 stimulation (Fig. 5B). The expression levels of pro-apoptotic genes, including apoptotic protease activating factor 1 (*Apaf-1*), *Bax*, *Casp7,* and *Casp12*, along with the S-100 family members *S100a8* and *S100a9*[28,29], were up-regulated, whereas those of anti-apoptotic genes *Bcl2l12*[30], *Rassf7*[31], *Herpud1*[32], *Nme6*[33], and *Foxa1*[34] were down-regulated in the livers of $Fgf4^{-/-}$ mice compared with those in $Fgf4^{fl/fl}$ controls upon ConA insult (Fig. 5C). In contrast, the expression levels of the aforementioned anti-apoptotic marker genes were increased, whereas those of pro-apoptotic *Apaf-1*, *Bax, Bid*, and *Casp7* were decreased in response to rFGF4 treatment (Fig. 5D). Among these genes, the balance between the pro-apoptotic members *Bax* and *Bid* and anti-apoptotic members *Bcl2l12* and *Bcl2l13* serves as a signal for the strict control of the opening of the mPTP, which regulates the initial phase of intrinsic apoptosis[35]. We did not detect any notable differences in the levels of expression of *Fas*, *Dr1*, *Fadd*, and *Tnfrsf14*, or downstream *Casp8* genes related to extrinsic apoptosis[36], with the exception of an increase in the expression of *Tnfrsf1a* upon hepatic FGF4 loss and a decrease upon rFGF4 treatment (Fig. S5G and H). Moreover, the intrahepatic protein levels of the pro-apoptotic factors Apaf-1, cleaved Casp9 (c-Casp9), Bax, and c-Casp3[28] were increased, whereas those of the anti-apoptotic factors cIAP-1, XIAP, and Bcl-2[37] were decreased (Fig. 5E). Conversely, treatment with exogenous rFGF4 effectively counteracted the changes in the expression levels of these intrinsic apoptosis-related factors (Fig. 5F). To determine whether the anti-apoptotic effect of FGF4 occurs directly in hepatocytes, we isolated primary hepatocytes. Western blot analysis revealed a trend in the change of the levels of apoptosis-related factors that was similar to those observed in whole tissues from both *Fgf4*-deficient and rFGF4-treated mice subjected to ConA-induced ILI (Fig. 5G and H).

Similarly, we found that in the S-100-induced ILI model, FGF4 deficiency increased the number of TUNEL-positive apoptotic cells (Supporting Information Fig. S6A) and protein levels of Apaf-1, c-Casp9, Bax, and c-Casp3, whereas decreased those of cIAP-1, XIAP, and Bcl-2 in the liver tissues (Fig. S6B and C) and isolated hepatocytes (Fig. S6D and E). Conversely, administration of rFGF4 to the S-100-induced ILI mice inhibited hepatocellular apoptosis and reversed the increase in the levels of apoptotic markers in the liver (Fig. S6F−H) and isolated hepatocytes (Fig. S6I and J). Conjointly, our results revealed that FGF4 predominantly inhibited the intrinsic apoptosis pathway, protecting hepatocytes and the liver from apoptotic death caused by an excessive immune response and inflammation in ILI mice.

3.6. Hepatic FGF4 inhibits apoptosis-evoked macrophage and T-cell infiltration under ILI conditions

The defective clearance of apoptotic cells is known to cause inflammatory responses and autoimmune diseases[38,39]. Apoptotic cells release various “find me” signals such as phosphatidylserine (PtdSer) and C-X3-C motif chemokine 1 (CX3CL1) to recruit macrophages, which infiltrate, recognise, and phagocytose apoptotic cells[39]. Using flow cytometry with 7-AAD and Annexin V, which are used to detect apoptotic fragmentations[40], we observed that FGF4 deficiency aggravated the ConA-induced PtdSer exposure and the progression of apoptosis in hepatocytes (Fig. 6A). Concurrently, the mRNA level of *Cx3cl1* was elevated in apoptotic hepatocytes (Fig. 6B). Furthermore, hepatic FGF4 deficiency promoted the recruitment of $F4/80^{+}CD11b^{+}$ macrophages (Fig. 6C and D). Upon assessing the co-localisation of F4/80, c-Casp3, and albumin by immunofluorescense staining, we found that the accumulation of infiltrated macrophages in apoptotic hepatocytes were more pronounced in the livers of FGF4-deficient mice than in floxed control mice with ConA-induced ILI (Fig. 6E). Macrophages are classified into the so-called M1 and M2 types. M1-type macrophages highly express major histocompatibility complex (MHC) and inflammatory factors, which promote inflammation, whereas M2 macrophages have powerful phagocytosis and clearance abilities, promoting tissue regeneration and anti-inflammation[41]. We observed that compared with floxed control mice, the proportion of $MHCII^{+}CD206^{-}$ M1-type macrophages was up-regulated in *Fgf4-LKO* ILI mice, whereas that of $MHCII^{-}CD206^{+}$ M2-type macrophages was significantly down-regulated (Fig. 6F and G). In line with these findings, the levels of high mobility group box protein 1 (HMGB1), a marker for inflammation-associated molecular patterns (DAPS) released by macrophages due to poor clearance of apoptotic cellular debris[42], were significantly elevated in FGF4-deficient mice (Fig. 6H). Correspondingly, the number of TCR $\beta^{+}CD3^{+}CD4^{+}$ T cells, which are thought to respond to phagocytic apoptotic fragments presented by macrophages through the MHCII-T-cell receptor (TCR)β pathway[43], was increased in the livers of *Fgf4-LKO* mice with ConA-induced ILI (Fig. 6I).

Conversely, rFGF4 treatment reduced the amount of Annexin V^{+} hepatocytes (Fig. 6J), indicating a reduction in PtdSer exposure to the exofacial leaflet of the plasma membrane. This was accompanied by the down-regulation of the mRNA levels of *Cx3cl1* (Fig. 6K) and the reduction in intrahepatic infiltration of

(I, R) Changes in the infiltration of TCR$\beta^{+}CD3^{+}CD4^{+}$ T-cells in livers of the indicated groups. (A, D, I, J, M, R) $n = 3$ per group; (F, O) $n = 3$−4 per group; (B, G, H, K, P, Q) $n = 6$ per group. Data are the mean ± SEM. (A, G, J, P) Ordinary two-way ANOVA followed by Tukey’s *post hoc* test; (B, D, H, I, K, M, Q, R) Two-tailed unpaired Student’s *t*-test. n.s., not significant.

M1-type macrophages (Fig. 6L−P). Furthermore, the increased proportion of M2-type macrophages suggested an enhanced clearance of apoptotic debris promoted by rFGF4 treatment (Fig. 6O and P), which correspondingly reduced the release of HMGB1 (Fig. 6Q) and intrahepatic infiltration of TCRβ^+CD3$^+$CD4$^+$ T-cells (Fig. 6R). Overall, these results suggested that under ILI conditions, intrahepatic FGF4 may serve to protect against hepatocyte apoptosis, which would otherwise increase the infiltration of macrophages and T-cells, aggravating inflammation and liver damage.

3.7. FGF4 activates the CaMKKβ/PINK1/Bcl-X_L pathway to regulate mPTP opening and intrinsic apoptosis in hepatocytes

Previous studies have suggested that the FGFR dimerization activates PLCγ to increase the cytoplasmic Ca^{2+} concentration ([Ca^{2+}]cyt), which stimulates the CaMKKβ/AMPK signalling pathway, thereby promoting significant hypoglycaemic, lipid-lowering, and anti-apoptotic effects[16,44]. The distribution of Ca^{2+} across different organelles and the subsequent activation of the CaMKKβ pathway are important factors affecting the opening of mPTP, which triggers the onset of endogenous apoptosis[26,45]. Our RNA-seq data suggest that the FGF4-activated pathway predominantly affects Ca^{2+} release (Fig. 5A and B), which coincides with the changes in the levels of mRNA expression of *Camkkβ/CAMK1D* (Fig. 7A and B). Measurement of intracellular Ca^{2+} flux revealed that FGF4 deficiency led to an increase in $[Ca^{2+}]_{mito}$ and a decrease in cytoplasmic free Ca^{2+} concentration ($[Ca^{2+}]_{cyt}$) in the hepatocytes of ConA-treated mice (Supporting Information Fig. S7A). By contrast, rFGF4 treatment reversed this trend in the intracellular free Ca^{2+} flux (Fig. S7B). PINK1, a homologue of CaMK1[46], is known to activate downstream target Bcl-X_L (Ser62)[47], which prevents mPTP opening[30,47,48]. We found that the mRNA levels of *Pink1* and *Bcl-X_L* were down-regulated under hepatic *Fgf4* deficiency but up-regulated upon rFGF4 administration (Fig. 7B). The phosphorylation levels of hepatocyte proteins CaMMKβ and PINK1 followed the same trend in the liver tissues of *Fgf4*-deficient and rFGF4-treated mice undergoing ConA-induced ILI (Fig. 7C and D). Furthermore, a same trend was observed in the changes of the mitochondrial activation of PINK1 and Bcl-X_L in response to hepatic FGF4 deficiency or rFGF4 treatment (Fig. 7E and F).

Notably, we found that CaMKKβ interacted with PINK1 in HEK293 cells as revealed by reciprocal co-immunoprecipitation (Fig. 7G). In addition, we detected that the fluorescence intensity of calcein acetoxymethyl ester (Calcein AM), a cell-permeant fluorescent indicator of mPTP opening[49], was decreased in the hepatocytes of *Fgf4*-deficient mice compared with those of *Fgf4$^{fl/fl}$* control mice under ILI conditions (Fig. 7H). Such a trend was reversed following rFGF4 treatment (Fig. 7I). Concordant with these observations, the FGF4 deficiency resulted in an increased efflux of Cyt *C* from the hepatocellular mitochondria to the cytoplasm (Fig. 7J), whereas such a "leakage" was prevented by exogenous rFGF4 treatment (Fig. 7K). Furthermore, we observed that the effects of rFGF4 in promoting Ca^{2+} efflux from mitochondria to the cytoplasm and the subsequent activation of the CaMKKβ/PINK1/BCL-X_L pathway were all abolished in the livers of *Fgfr4-LKD* mice (Fig. S7C and Fig. 7L and M).

3.8. Pharmacological rFGF4 protects the liver from ILI dependently on the activation of CaMKKβ-Pink1-Bcl-XL signal pathway

To better understand the potential role of the CaMKKβ-PINK1-Bcl-X_L signalling pathway in mediating the hepatoprotective effects of FGF4 in ILI, we developed a *Camkkβ-KO* mouse model (Supporting Information Fig. S8A and B) in conjunction with AAV8-TBG-mediated shRNA knock-down of *Pink1* (*Pink1-LKD*) (Fig. S8C−E) under ConA challenge or rFGF4 treatment. We detected that the expression of CaMKKβ was minimized in the hepatocytes of *Camkkβ-KO* mice. The *Camkkβ* deficiency aggravated the ConA-induced hepatocellular death and rescinded the protective effects of rFGF4 against liver injury (Fig. 8A). This was accompanied by sustained increases in the levels of serum ALT and AST (Fig. 8B), serum pro-inflammatory factors (Fig. 8C), and intrahepatic F4/80$^+$ macrophage infiltration (Fig. 8D). Of note, *Camkkβ* deficiency also abolished the ability of rFGF4 to reduce CD4$^+$ T-cell infiltration (Fig. 8E). Moreover, the loss of CaMKKβ abrogated the response of hepatocytes and mitochondria to rFGF4 treatment and the activation of downstream PINK1 and Bcl-X_L (Supporting Information Fig. S9A−D). The inhibitory effects of rFGF4 on mPTP opening (Fig. S9E) and Cyt *C* efflux (Fig. S9F) were similarly blunted, leading to elevated hepatocellular apoptosis that was intractable to rFGF4 treatment in the livers of ILI mice (Fig. S9G and H).

We also found that the knock-down of *Pink1* negated the rFGF4-promoted protection of the liver against ConA-induced damage and focal cell death (Fig. 8F). Coincidently, serum levels of liver enzymes (ALT and AST) (Fig. 8G) and pro-inflammatory factors (IL-1β, IL-6, IFN-γ, and TNF-α) (Fig. 8J) and intrahepatic macrophage infiltration (Fig. 8I) remained consistently high even under rFGF4 treatment. The infiltration of CD4$^+$ T-cells also remained high and unaltered (Fig. 8J). Furthermore, rFGF4 treatment failed to mitigate the reduction in phosphorylated Bcl-X_L in mitochondria caused by *Pink1* knock-down (Supporting Information Fig. S10A). Consequently, neither the mPTP opening nor the subsequent efflux of Cyt *C* was restored (Fig. S10B and C), retaining high levels of hepatocellular apoptosis (Fig. S10D and E). Thus, our data suggested that rFGF4 inhibits hepatocellular intrinsic apoptosis by triggering the CaMKK2/PINK1/Bcl-X_L signalling downstream of FGFR4 (Fig. 8K).

4. Discussion

Immune-mediated liver injury is a prevalent global health problem with an estimated incidence of 15−20 cases per 100,000 individuals, among which the drug/chemical-induced ILI accounts for more than half of the cases of acute liver failure in Western countries[2]. Apoptosis is the main cause of cell death in ILI and an important cause of the excessive or exacerbated immune response; however, no drugs specifically targeting hepatocellular apoptosis with hepatoprotective effects are currently available. Thus, managing ILI remains a significant challenge in the clinic. In this study, we found that FGF4 is an inducible factor in hepatocytes in response to liver injury caused by AIH and in animal models of ILI. Mechanistically, we found that the expression of hepatic *Fgf4*

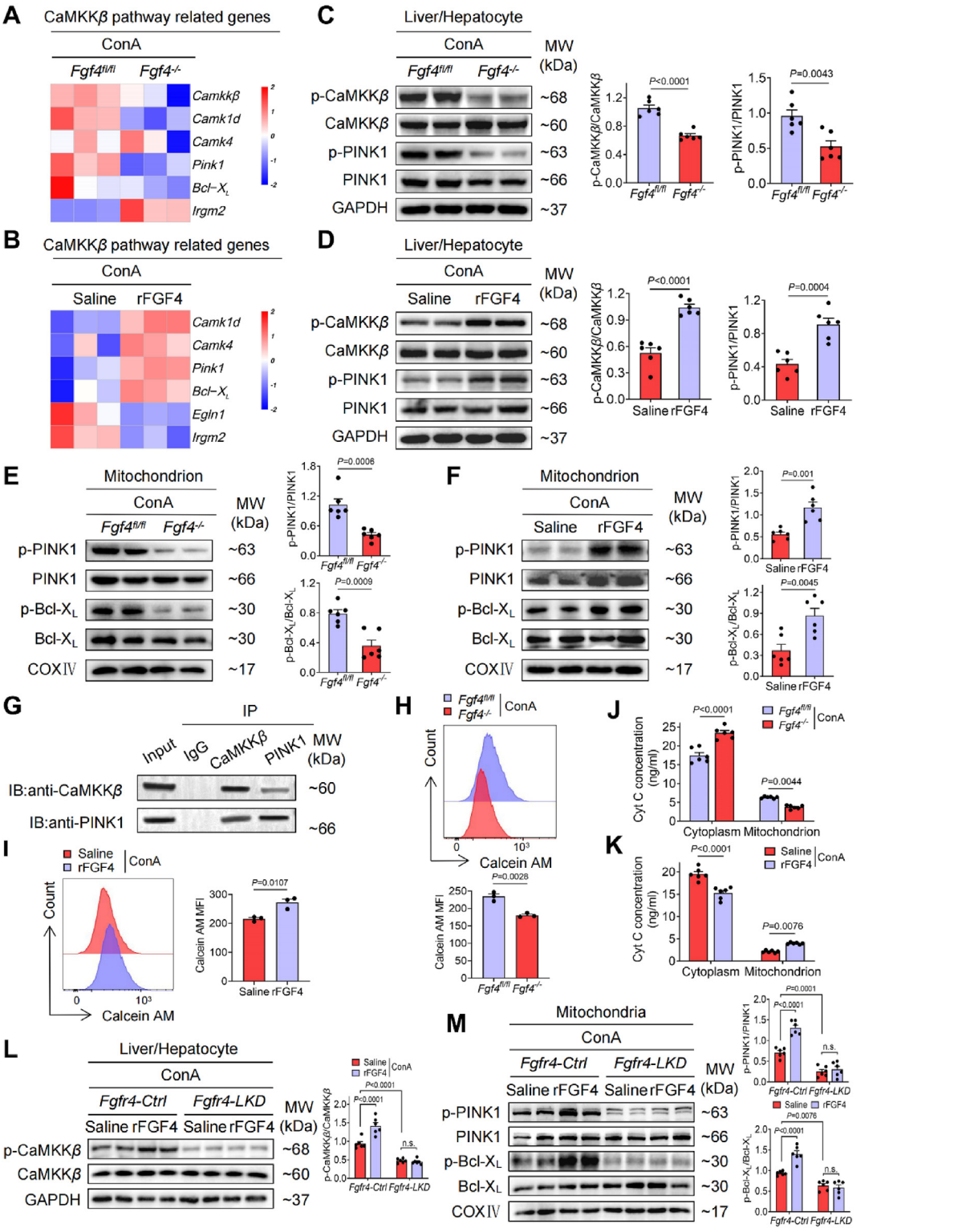

Figure 7 FGF4 regulates mitochondrial mPTP opening and Cyt *C* efflux through the CaMKKβ/PINK1/Bcl-X_L pathway. (A, B) Heatmap representation of differentially expressed genes involved in the CaMKKβ pathway upon hepatic FGF4 deficiency or rFGF4 treatment in liver tissues from the indicated groups based on RNA-seq data. (C, D) Western blot analysis of proteins involved in the CaMKKβ pathway in hepatocytes isolated from the indicated groups. (E, F) Western blot analysis of proteins downstream of the CaMKKβ pathway in mitochondria isolated from hepatocytes of the indicated groups. (G) Reciprocal co-immunoprecipitations of CaMKKβ and PINK1 in HEK293 cells. (H, I) Changes in the Calcein AM^+ hepatocyte population isolated from the indicated groups reflecting mPTP opening. (J, K) Change in the flux of Cyt *C* in hepatocellular cytoplasm and mitochondria isolated from the indicated groups. (L) Western blot analysis of CaMKKβ phosphorylation levels in hepatocytes isolated from the indicated groups. (M) Western blotting analysis of proteins related to the PINK1/BCL-X_L pathway in hepatocellular mitochondria isolated from livers of the indicated groups. (A, B, H, I) $n = 3$ per group; (C−F, J−M) $n = 6$ per group. Data are the mean ± SEM. (C−F, H, I) Two-tailed unpaired Student's *t*-test. (J, K) Ordinary two-way ANOVA followed by Sidak *post hoc* test. (L, M) Ordinary two-way ANOVA followed by Tukey's *post hoc* test. n.s., not significant.

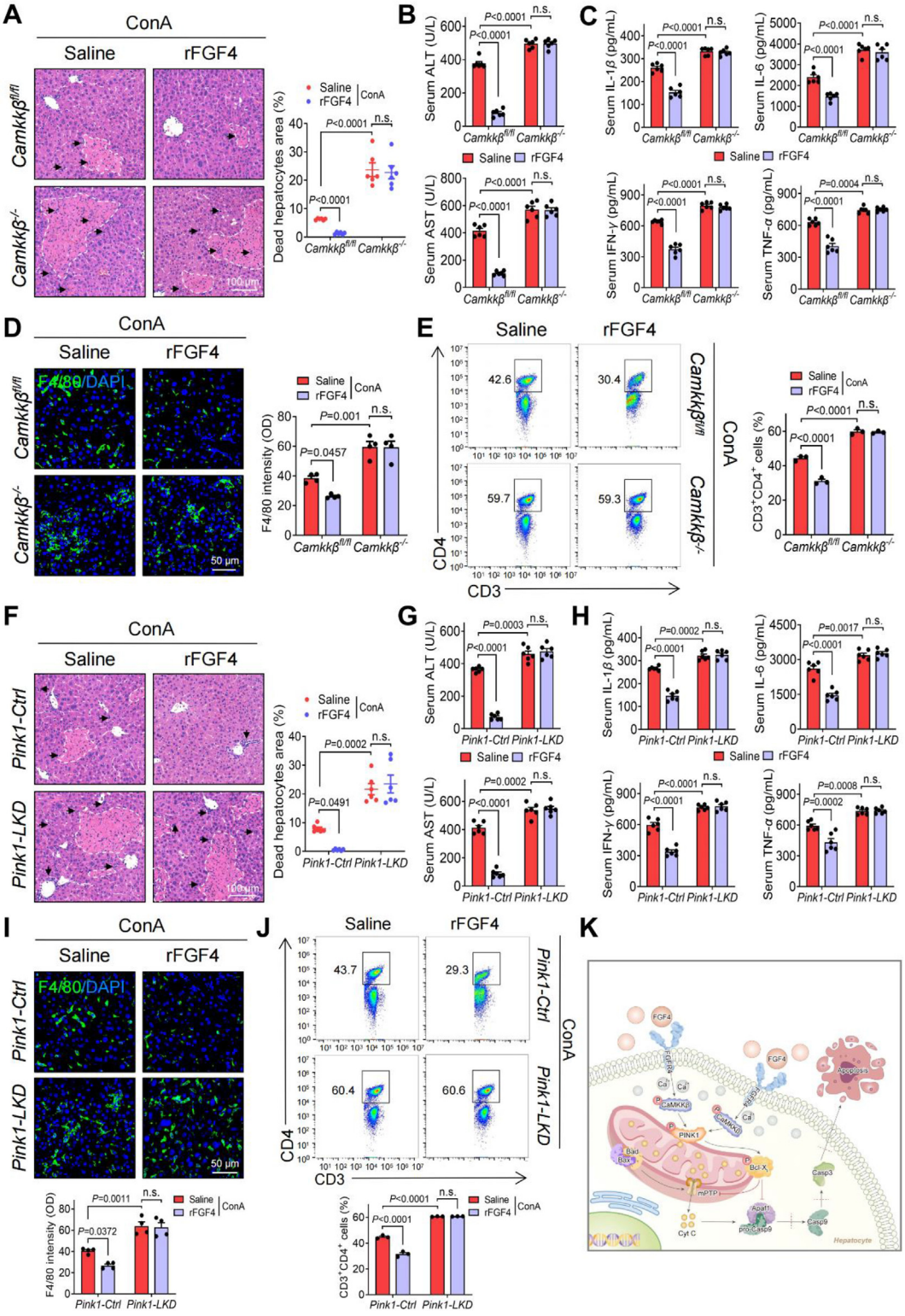

Figure 8 Activation of the CaMKKβ/PINK1 pathway by FGF4 underlies its protective effect against ILI. (A, F) Representative H&E-stained images and statistical analysis (%) of focal hepatocyte death in liver tissues from the indicated groups. Areas of dead hepatocytes are circled with white dotted trace lines, and lymphocytes are indicated by black arrows. Scale bar = 100 μm. (B, G) Serum levels of ALT (upper) and AST (lower) in the indicated groups. (C, H) Serum levels of pro-inflammatory cytokines in the indicated groups. (D, I) Representative images and quantification of F4/80 (green) immunofluorescent stains with DAPI (blue) counterstains in liver sections from the indicated groups. Scale bar = 50 μm. (E, J) Changes in the infiltration of $CD3^+CD4^+$ T-cells in livers of the indicated groups. (K) Graphic model depicting the role of FGF4 in protecting the liver from ConA-induced ILI pathologies by activating the CaMKKβ-PINK1-Bcl-X_L signalling axis. (A−C, F−H) $n = 6$ per group; (D, I) $n = 4$ per group; (E, J) $n = 3$ per group. Data are the mean ± SEM. (A−J) Ordinary two-way ANOVA followed by Tukey's *post hoc* test. n.s., not significant.

is likely under the transcriptional control of NUR77 or ATF3, both of which have previously been shown to regulate the transcription of other FGF family members by binding to the response elements such as NUR77/NGFI-B DNA-binding element (NBRE) in the promoter region of the target genes[21–23]. It remains to be investigated whether NUR77 and ATF3 regulate the transcription of FGF4 by a similar mechanism.

We also found that, under ILI conditions, hepatocytes but not macrophages, T-cells, or NK cells are the main target of FGF4. Hepatic FGF4 deficiency exacerbated the apoptosis of hepatocytes induced by both ConA and S-100 treatments, leading to an increase in the infiltration of M1-type macrophages but a decrease of M2-type macrophages. Consequently, this resulted in an inefficient removal of apoptotic fragments presented to $CD4^+$ T-cells *via* the MHCII/TCRβ pathway, thereby intensifying inflammation, immunity responses, and liver damage[38]. By contrast, treatment with exogenous FGF4 in both acute and chronic settings mitigated the aggravation of hepatocyte death, the significant infiltration of immune cells, and inflammation. This was accompanied by a return to normal levels of liver enzymes ALT and AST, as well as a battery of pro-inflammatory cytokines in both ConA- and S-100-induced ILI. Therefore, our study suggested that the protective effect of FGF4 on ILI can be attributed to its direct protection of hepatocytes from inflammatory assaults triggered by intrahepatic immune disorders, thereby disrupting the detrimental cycle of apoptosis-immune disorders.

We observed that intrinsic apoptosis, which is associated with the opening of mPTP, $[Ca^{2+}]_{mito}$ level and the efflux of Cyt *C*, is the main pathway through which FGF4 regulates hepatocyte death in ILI mice. No major changes were observed in factors involved in the extrinsic apoptotic pathway. Hepatic FGF4 deficiency further promoted mPTP opening and mitochondrial Ca^{2+} influx in ILI-plagued hepatocytes, which were accompanied by an increase in the levels of apoptotic factors and a decrease in those of anti-apoptotic factors, thereby exacerbating hepatocyte apoptosis and liver damage. On the contrary, acute and chronic administrations of exogenous FGF4 in the subsiding phase of the induction of hepatic FGF4 during ILI pathogenesis effectively counteracted such adaptive and adverse changes in mitochondrial membrane potential and levels of regulatory factors associated with the intrinsic apoptotic pathway, leading to a significant attenuation of hepatocellular apoptotic death and liver damage. This was in accordance with the observations that apoptosis strongly influenced the ILI-induced formation of globules of dead hepatocytes and cell fragments[5,6]. Thus, our results indicated that hepatic and pharmacological FGF4 predominantly normalizes mPTP opening, leading to protection of the hepatocytes and liver from apoptotic death and damage caused by the insult of excessive immune reactivity and inflammation.

The opening of mPTP as the initiation phase of endogenous apoptosis is known to be tightly regulated by Ca^{2+} signalling[26,27] and the equilibrium of the Bcl-2 family members[30,35]. Of note, FGF/FGFR signalling has been shown to have an anti-apoptotic role *via* the activation of the PLC-γ pathway, which up-regulates $[Ca^{2+}]_{cyto}$ and stimulates the CaMKKβ/AMPK signalling pathway. In line with the altered flux of $[Ca^{2+}]$ between the cytosol and mitochondria and the significant changes in the Ca^{2+}-associated signalling pathway in ConA-induced ILI, hepatic FGF4 deficiency led to an inhibition of FGFR4 while exogenous rFGF4 treatment led to an activation of FGFR4. This, in turn, activated the $[Ca^{2+}]$-sensitive CaMKKβ, leading to changes in the activation of downstream PINK1 and Bcl-X_L that have a strong impact on the apoptosis process[30,47,48]. In contrast, knockdown of FGFR4 specifically in hepatocytes counteracted the protective effect of rFGF4 against ILI. PINK1, a homologue of CaMK1 downstream of CaMKK, in known to be phosphorylated to promote the activation of Bcl-X_L, thereby protecting cells from apoptotic death[46]. Bcl-X_L proteins can also inhibit apoptosis caused by calcium overload in mitochondria by promoting Ca^{2+} efflux from mitochondria[50] and Ca^{2+} uptake in the endoplasmic reticulum[51]. Notably, we observed that hepatocyte-specific ablation or knockdown of either CaMKKβ or PINK1 reduced the effects of FGF4 on Bcl-X_L activation, mPTP opening, mitochondrial Cyt *C* efflux, intrinsic apoptosis regulators, intrahepatic immune cell infiltration, and liver injury caused by the ConA or S-100 immunogenic challenge.

5. Conclusions

In summary, our study demonstrated that hepatic FGF4 activates the FGFR4-CaMKKβ-PINK1-Bcl-X_L signalling pathway to inhibit hepatocellular intrinsic apoptosis in association with mitochondrial membrane potential and integrity, thereby protecting the liver from immune disorder-induced liver damage and functional perturbation. This expands the horizon of the physiopathological roles of FGF4 in liver homeostasis, shedding new light on potential strategies for the pharmacotherapeutic intervention of immune disorder-associated hepatic diseases.

Acknowledgments

We appreciate the financial support from the National Natural Science Foundation of China (82070593, 92057122, 80223003, 82002965 to Yongping Chen, Zhifeng Huang, Xiaokun Li, and Lintao Song), Key Project of Zhejiang Provincial Natural Science Foundation (LD21H030002, DQ24H310001 to Yongping Chen and Zhifeng Huang, China), and Key Project from Science Technology Department of Wenzhou (ZY2021022 to Zhifeng Huang, China).

Author contributions

Yongping Chen, Zhifeng Huang, and Tongtong Pan conceived the project and designed experiments. Tongtong Pan, Liang Xu, Lu Shi, Xiong Ma, Liya Zhou, Luyao Wang, Jiaojiao Wang, Guoqing Zhu, Dazhi Chen, Lingtao Song and Xiaomin Pan performed experiments, analyzed data, and participated in discussion of the results. Tongtong Pan, Xiaodong Wang, and Yongping Chen applied for clinical ethics and provided patient samples. Tongtong Pan, Zhifeng Huang, and Yongde Luo. wrote this manuscript.

Conflicts of interest

The authors declare no conflict of interest.

Appendix A. Supporting information

Supporting data to this article can be found online at https://doi.org/10.1016/j.apsb.2023.12.012.

References

1. Robinson MW, Harmon C, O'Farrelly C. Liver immunology and its role in inflammation and homeostasis. *Cell Mol Immunol* 2016;**13**:267−76.
2. Hoofnagle JH, Björnsson ES. Drug-induced liver injury - types and phenotypes. *N Engl J Med* 2019;**38**:264−73.
3. Longhi MS, Ma Y, Mieli-Vergani G, Vergani D. Aetiopathogenesis of autoimmune hepatitis. *J Autoimmun* 2010;**34**:7−14.
4. Mieli-Vergani G, Vergani D, Czaja AJ, Manns MP, Krawitt EL, Vierling JM, et al. Autoimmune hepatitis. *Nat Rev Dis Prim* 2018;**4**:18017.
5. Tsikrikoni A, Kyriakou DS, Rigopoulou EI, Alexandrakis MG, Zachou K, Passam F, et al. Markers of cell activation and apoptosis in bone marrow mononuclear cells of patients with autoimmune hepatitis type 1 and primary biliary cirrhosis. *J Hepatol* 2005;**42**:393−9.
6. Bai J, Odin JA. Apoptosis and the liver: relation to autoimmunity and related conditions. *Autoimmun Rev* 2003;**2**:36−42.
7. Kerr JF, Cooksley WG, Searle J, Halliday JW, Halliday WJ, Holder L, et al. The nature of piecemeal necrosis in chronic active hepatitis. *Lancet* 1979;**2**:827−8.
8. Harrington C, Krishnan S, Mack CL, Cravedi P, Assis DN, Levitsky J. Noninvasive biomarkers for the diagnosis and management of autoimmune hepatitis. *Hepatology* 2022;**76**:1862−79.
9. Ornitz DM, Itoh N. Fibroblast growth factors. *Genome Biol* 2001;**2**. REVIEWS3005.
10. Beenken A, Mohammadi M. The FGF family: biology, pathophysiology and therapy. *Nat Rev Drug Discov* 2009;**8**:235−53.
11. Ye D, Wang Y, Li H, Jia W, Man K, Lo CM, et al. Fibroblast growth factor 21 protects against acetaminophen-induced hepatotoxicity by potentiating peroxisome proliferator-activated receptor coactivator protein-1α-mediated antioxidant capacity in mice. *Hepatology* 2014;**60**:977−89.
12. Li S, Zhu Z, Xue M, Pan X, Tong G, Yi X, et al. The protective effects of fibroblast growth factor 10 against hepatic ischemia−reperfusion injury in mice. *Redox Biol* 2021;**40**:101859.
13. Takase HM, Itoh T, Ino S, Wang T, Koji T, Akira S, et al. FGF7 is a functional niche signal required for stimulation of adult liver progenitor cells that support liver regeneration. *Genes Dev* 2013;**27**:169−81.
14. Song L, Wang L, Hou Y, Zhou J, Chen C, Ye X, et al. FGF4 protects the liver from nonalcoholic fatty liver disease by activating the AMP-activated protein kinase-Caspase 6 signal axis. *Hepatology* 2022;**76**:1105−20.
15. Manns MP, Lohse AW, Vergani D. Autoimmune hepatitis–update 2015. *J Hepatol* 2015;**62**:S100−11.
16. Ying L, Wang L, Guo K, Hou Y, Li N, Wang S, et al. Paracrine FGFs target skeletal muscle to exert potent anti-hyperglycemic effects. *Nat Commun* 2021;**12**:7256.
17. Cossarizza A, Chang HD, Radbruch A, Akdis M, Andrä I, Annunziato F, et al. Guidelines for the use of flow cytometry and cell sorting in immunological studies. *Eur J Immunol* 2017;**47**:1584−797.
18. Tiegs G, Hentschel J, Wendel A. A T cell-dependent experimental liver injury in mice inducible by concanavalin A. *J Clin Invest* 1992;**90**:196−203.
19. Lohse AW, Manns M, Dienes HP, Meyer zum Büschenfelde KH, Cohen IR. Experimental autoimmune hepatitis: disease induction, time course and T-cell reactivity. *Hepatology* 1990;**11**:24−30.
20. Inagaki T, Dutchak P, Zhao G, Ding X, Gautron L, Parameswara V, et al. Endocrine regulation of the fasting response by PPARalpha-mediated induction of fibroblast growth factor 21. *Cell Metabol* 2007;**5**:415−25.
21. Ahuja P, Bi X, Ng CF, Tse MCL, Hang M, Pang BPS, et al. Src homology 3 domain binding kinase 1 protects against hepatic steatosis and insulin resistance through the Nur77-FGF21 pathway. *Hepatology* 2023;**77**:213−29.
22. Min AK, Bae KH, Jung YA, Choi YK, Kim MJ, Kim JH, et al. Orphan nuclear receptor Nur77 mediates fasting-induced hepatic fibroblast growth factor 21 expression. *Endocrinology* 2014;**155**:2924−31.
23. Xu Y, Li Y, Jadhav K, Pan X, Zhu Y, Hu S, et al. Hepatocyte ATF3 protects against atherosclerosis by regulating HDL and bile acid metabolism. *Nat Metab* 2021;**3**:59−74.
24. Kim KH, Jeong YT, Oh H, Kim SH, Cho JM, Kim YN, et al. Autophagy deficiency leads to protection from obesity and insulin resistance by inducing Fgf21 as a mitokine. *Nat Med* 2013;**19**:83−92.
25. Mfopou JK, Chen B, Mateizel I, Sermon K, Bouwens L. Noggin, retinoids, and fibroblast growth factor regulate hepatic or pancreatic fate of human embryonic stem cells. *Gastroenterology* 2010;**138**:2233−45.
26. Bauer TM, Murphy E. Role of Mitochondrial calcium and the permeability transition pore in regulating cell death. *Circ Res* 2020;**126**:280−93.
27. Rizzuto R, De Stefani D, Raffaello A, Mammucari C. Mitochondria as sensors and regulators of calcium signalling. *Nat Rev Mol Cell Biol* 2012;**13**:566−78.
28. Wu CC, Lee S, Malladi S, Chen MD, Mastrandrea NJ, Zhang Z, et al. The Apaf-1 apoptosome induces formation of caspase-9 homo- and heterodimers with distinct activities. *Nat Commun* 2016;**7**:13565.
29. Li Y, Chen B, Yang X, Zhang C, Jiao Y, Li P, et al. S100a8/a9 signaling causes mitochondrial dysfunction and cardiomyocyte death in response to ischemic/reperfusion Injury. *Circulation* 2019;**140**:751−64.
30. Hollville E, Carroll RG, Cullen SP, Martin SJ. Bcl-2 family proteins participate in mitochondrial quality control by regulating Parkin/-PINK1-dependent mitophagy. *Mol Cell* 2014;**55**:451−66.
31. Takahashi S, Ebihara A, Kajiho H, Kontani K, Nishina H, Katada T. RASSF7 negatively regulates pro-apoptotic JNK signaling by inhibiting the activity of phosphorylated-MKK7. *Cell Death Differ* 2011;**18**:645−55.
32. Paredes F, Parra V, Torrealba N, Navarro-Marquez M, Gatica D, Bravo-Sagua R, et al. HERPUD1 protects against oxidative stress-induced apoptosis through downregulation of the inositol 1,4,5-trisphosphate receptor. *Free Radic Biol Med* 2016;**90**:206−18.
33. Proust B, Radić M, Vidaček NŠ, Cottet C, Attia S, Lamarche F, et al. NME6 is a phosphotransfer-inactive, monomeric NME/NDPK family member and functions in complexes at the interface of mitochondrial inner membrane and matrix. *Cell Biosci* 2021;**11**:195.
34. Liu DW, Zhang JH, Liu FX, Wang XT, Pan SK, Jiang DK, et al. Silencing of long noncoding RNA PVT1 inhibits podocyte damage and apoptosis in diabetic nephropathy by upregulating FOXA1. *Exp Mol Med* 2019;**51**:1−15.
35. Singh R, Letai A, Sarosiek K. Regulation of apoptosis in health and disease: the balancing act of BCL-2 family proteins. *Nat Rev Mol Cell Biol* 2019;**20**:175−93.
36. Rudel T, Kepp O, Kozjak-Pavlovic V. Interactions between bacterial pathogens and mitochondrial cell death pathways. *Nat Rev Microbiol* 2010;**8**:693−705.
37. Beug ST, Cheung HH, LaCasse EC, Korneluk RG. Modulation of immune signalling by inhibitors of apoptosis. *Trends Immunol* 2012;**33**:535−45.
38. Nagata S. Apoptosis and clearance of apoptotic cells. *Annu Rev Immunol* 2018;**36**:489−517.
39. Medina CB, Ravichandran KS. Do not let death do us part: 'find-me' signals in communication between dying cells and the phagocytes. *Cell Death Differ* 2016;**23**:979−89.
40. Koopman G, Reutelingsperger CP, Kuijten GA, Keehnen RM, Pals ST, van Oers MH. Annexin V for flow cytometric detection of phosphatidylserine expression on B cells undergoing apoptosis. *Blood* 1994;**84**:1415−20.
41. Porta C, Riboldi E, Ippolito A, Sica A. Molecular and epigenetic basis of macrophage polarized activation. *Semin Immunol* 2015;**27**:237−48.
42. Chen R, Kang R, Tang D. The mechanism of HMGB1 secretion and release. *Exp Mol Med* 2022;**54**:91−102.
43. Germic N, Frangez Z, Yousefi S, Simon HU. Regulation of the innate immune system by autophagy: monocytes, macrophages, dendritic cells and antigen presentation. *Cell Death Differ* 2019;**26**:715−27.

44. Huang Z, Marsiglia WM, Basu Roy U, Rahimi N, Ilghari D, Wang H, et al. Two FGF receptor kinase molecules act in concert to recruit and transphosphorylate phospholipase Cγ. *Mol Cell* 2016;**61**:98−110.
45. Bonora M, Giorgi C, Pinton P. Molecular mechanisms and consequences of mitochondrial permeability transition. *Nat Rev Mol Cell Biol* 2022;**23**:266−85.
46. Abou-Sleiman PM, Muqit MMK, McDonald NQ, Yang YX, Gandhi S, Healy DG, et al. A heterozygous effect for PINK1 mutations in Parkinson's disease? *Ann Neurol* 2006;**60**:414−9.
47. Arena G, Gelmetti V, Torosantucci L, Vignone D, Lamorte G, De Rosa P, et al. PINK1 protects against cell death induced by mitochondrial depolarization, by phosphorylating Bcl-xL and impairing its pro-apoptotic cleavage. *Cell Death Differ* 2013;**20**:920−30.
48. Gautier CA, Giaime E, Caballero E, Núñez L, Song Z, Chan D, et al. Regulation of mitochondrial permeability transition pore by PINK1. *Mol Neurodegener* 2012;**7**:22.
49. Wang XM, Terasaki PI, Rankin GW, Chia D, Zhong HP, Hardy S. A new microcellular cytotoxicity test based on calcein AM release. *Hum Immunol* 1993;**37**:264−70.
50. Huang H, Hu X, Eno CO, Zhao G, Li C, White C. An interaction between Bcl-xL and the voltage-dependent anion channel (VDAC) promotes mitochondrial Ca^{2+} uptake. *J Biol Chem* 2013;**288**:19870−81.
51. Rosa N, Ivanova H, Wagner 2nd LE, Kale JAO, La Rovere R, Welkenhuyzen K, et al. Bcl-xL acts as an inhibitor of IP(3)R channels, thereby antagonizing Ca^{2+}-driven apoptosis. *Cell Death Differ* 2022;**29**:788−805.